ISTANBUL TECHNICAL UNIVERSITY ★ GRADUATE SCHOOL OF SCIENCE ENGINEERING AND TECHNOLOGY

DYNAMIC RESPONSE ANALYSIS OF A FLOATING PLATFORM FOR OFFSHORE WIND TURBINES

M.Sc. THESIS

Enes TUNCA

Department of Naval Architecture and Marine Engineering

Naval Architecture and Marine Engineering Programme

AUGUST 2017

ISTANBUL TECHNICAL UNIVERSITY ★ GRADUATE SCHOOL OF SCIENCE ENGINEERING AND TECHNOLOGY

DYNAMIC RESPONSE ANALYSIS OF A FLOATING PLATFORM FOR OFFSHORE WIND TURBINES

M.Sc. THESIS

Enes TUNCA
(508141003)

Department of Naval Architecture and Marine Engineering

Naval Architecture and Marine Engineering Programme

Thesis Advisor: Assoc. Prof. Bahadır UĞURLU

AUGUST 2017

ISTANBUL TEKNİK ÜNİVERSİTESİ ★ FEN BİLİMLERİ ENSTİTÜSÜ

YÜZER RÜZGAR TÜRBİNİ PLATFORMLARININ DİNAMİK TEPKİ ANALİZİ

YÜKSEK LİSANS TEZİ

Enes TUNCA
(508141003)

Gemi İnşaatı ve Gemi Makinaları Mühendisliği Anabilim Dalı

Gemi İnşaatı ve Gemi Makinaları Mühendisliği Programı

Tez Danışmanı: Doç. Dr. Bahadır UĞURLU

AĞUSTOS 2017

Enes TUNCA, an M-.Sc. student of ITU Graduate School of Science Engineering and Technology student ID **508141003**, successfully defended the thesis/dissertation entitled **"DYNAMIC RESPONSE ANALYSIS OF A FLOATING PLATFORM FOR OFFSHORE WIND TURBINES"**, which he prepared after fulfilling the requirements specified in the associated legislations, before the jury whose signatures are below.

Thesis Advisor :   **Assoc. Prof. Bahadır Uğurlu**   ....
Istanbul Technical University

Jury Members :   **Prof. Şakir Bal**   ....
Istanbul Technical University

Assoc. Prof. İsmail BAYER   ....
Yıldız Technical University

Date of Submission : 14 August 2017
Date of Defense   : 17 August 2017

To my family and twin nieces,

Serra & Feyza,

"So, when you have finished, immediately strive hard to do next. (Al-Inshirah, 7)"

FOREWORD

I would like to express my sincere thanks and appreciation to my advisor Assoc. Prof. Bahadır Uğurlu for his friendship and patiently support and to İsmail Kahraman who can always give an advice about any issue. I appreciate to all of my co-workers for their valuable support. Besides, I would like to thanks to the National Renewable Energy Laboratory (NREL) for providing the public documentation about wind energy.

I extend my sincerest gratitude to my parents giving me the morality of striving to make the best.

August 2017

Enes TUNCA
Naval Architect and Marine Engineer

TABLE OF CONTENTS

ABBREVIATIONS

BE	**:** Boundary Element
BEM	**:** Boundary Element Method
BEMt	**:** Blade Element Momentum Theory
BIE	**:** Boundary Integral Equation
COG	**:** Center of Gravity
DOF	**:** Degree of Freedom
EWEA	**:** European Wind Energy Association
FE	**:** Finite Element
FEM	**:** Finite Element Method
FOWT	**:** Floating Offshore Wind Turbine
IRF	**:** Impulse Response Function
NMRI	**:** National Maritime Research Institute
NREL	**:** National Renewable Energy Laboratory
RAO	**:** Response Amplitude Operator
RNA	**:** Rotor-Nacelle Assembly
TLP	**:** Tension Leg Platform
VLFS	**:** Very Large Floating Structure
WGN	**:** White Gaussian Noise

SYMBOLS

A	: Hydrodynamic added mass matrix
$\mathbf{A}_\infty$	: Infinite frequency limit of the hydrodynamic added mass
A	: Rotor area
a	: Generalized mass matrix
B	: Hydrodynamic damping matrix
b	: Generalized damping matrix
C	: Hydrostatic stiffness matrix
$\mathbf{C}_V$	: Damping matrix
C_D	: Non-dimensional drag coefficient
C_L	: Non-dimensional lift coefficient
C_P	: Non-dimensional power coefficient
c	: Generalized stiffness matrix
E	: Young modulus
F	: Force vector
F_x	: Axial force
f	: Generalized external force vector
$\mathbf{f}_A$	: Generalized aerodynamic force vector
$\mathbf{f}_H$	: Generalized hydrodynamic force vector
$\mathbf{f}_{HS}$	: Generalized hydrostatic force vector
$\mathbf{f}_W$	: Wave excitation force vector
$\mathbf{f}_R$	: Radiation force vector
G	: Free surface Green function
g	: Gravitational acceleration
I	: Moment of inertia
K	: Stiffness matrix
K_{ij}	: Impulse response function
k	: Wave number
M	: Mass matrix
M_x, M_y, M_{xy}	: Torque components
m	: Mass
N_i	: Shape function
n	: Normal vector
P	: Pressure
$\ddot{\mathbf{p}}, \dot{\mathbf{p}}, \mathbf{p}$	: Principle coordinate vectors
Q	: Tip-loss factor
$\ddot{\mathbf{q}}, \dot{\mathbf{q}}, \mathbf{q}$	: Acceleration, velocity and displacement
r	: Position vector
S_f, S_w	: Free surface, wetted surface
$S_\zeta^{2-Sided}$	: Two-sided power spectral density
T	: Transformation matrix
T	: Torque

t	**:** Time
U	**:** Modal matrix
u	**:** Mode shape vector
U	**:** Wind speed
W	**:** Fourier transform a white Gaussian noise time-series
x	**:** Position vector, dependent variable of the state-space model
X	**:** Complex wave excitation
V	**:** Airflow velocity
v	**:** Velocity vector
z_r	**:** Roughness length
α	**:** Incident wave angle, induction factor
β	**:** Angle between wind and airflow over airfoil
δ	**:** Dirac delta
$\varepsilon_x,\ \varepsilon_y,\ \varepsilon_{xy}$	**:** Strain components
Φ	**:** Velocity potential
Φ_R	**:** Radiation velocity potential
Φ_D	**:** Diffraction velocity potential
Φ_I	**:** Incident wave velocity potential
Φ_S	**:** Scattered wave velocity potential
Γ	**:** Domain surface
$\lambda,\ \lambda_h,\ \lambda_r$	**:** Blade, hub and local tip speed ratio
ρ	**:** Density
σ'	**:** Blade local solidity
$\sigma_x,\ \sigma_y,\ \sigma_{xy}$	**:** Stress components
ω	**:** Frequency, wake rotation velocity
ξ	**:** Position vector
Ω	**:** Problem domain, blade rotation velocity
Ξ	**:** Exciting force vector
Ξ_H	**:** Wave-exciting force vector
ζ	**:** Wave amplitude

LIST OF TABLES

LIST OF FIGURES

DYNAMIC RESPONSE ANALYSIS OF A FLOATING PLATFORM FOR OFFSHORE WIND TURBINES

SUMMARY

In recent years, studies demonstrating the potential of the offshore wind energy have shown that the installation site of the wind turbines needs to be extended to areas farther from the shore. However, bottom founded type offshore wind turbines have limited the installation site to the near-shore areas, so far. Making more use of the wind energy source is possible through the floating type offshore wind turbines. Due to the extreme loads, comprehensive response analysis of the floating offshore wind turbines under combined wave and wind excitation is essential during the initial design.

In this study, the response analysis of the large-scale floating platform carrying two wind turbines is performed under combined wave and wind loads. It is well accepted that the investigation of the rigid body motions of the floater is sufficient in response analysis; however, the elastic motions of the floater should be considered in present study due to its dimensions.

In order to analyze the aero-hydro-elastic response of the floater, firstly the dynamic characteristics are determined by the finite element analysis by considering that the response of the structure can be represented by its dynamic characteristics. The rotor-nacelle assembly of the wind turbine is imitated by a concentrated mass with rotational inertia in finite element analysis. Hydrodynamic radiation and wave forces in frequency domain are computed according to the dynamic characteristics by using the boundary element method and transformed to their time domain representation by the convolution of the radiation impulse response function and using the sine transformation, respectively. The sea state is modeled by using the Pierson-Moskowitz wave spectra. The aerodynamic forces are obtained by considering the steady wind condition and using the blade element momentum theory. The time domain response of the structure is acquired by the time integration of the equation of motion.

YÜZER RÜZGAR TÜRBİNİ PLATFORMLARININ DİNAMİK TEPKİ ANALİZİ

ÖZET

Son yıllarda, rüzgâr enerjisi, yenilenebilir enerji kaynakları arasında en çok yatırım yapılan, geleceğin enerji kaynağı çözümü haline gelmiştir. Bu bağlamda, rüzgâr enerjisinden daha uygun maliyetle faydalanılması için çok sayıda mühendislik çalışması literatüre kazandırılmıştır. Açık denizlerdeki rüzgâr enerjisi potansiyelini ortaya koyan çalışmalar, rüzgâr türbinlerinin inşa sahasının kıyıdan uzak bölgelere genişletilmesi gerekliliğini ortaya çıkarmıştır. Bununla birlikte, denizlerde inşa edilen rüzgâr türbinlerinin deniz dibinde bir temel ile desteklenmesi gerekliliği, günümüze kadarki inşa sahalarını kıyıya yakın bölgelere kısıtlamıştır. Daha derin denizlerdeki enerji potansiyelinden faydalanabilmek, ancak yüzer rüzgâr türbinleri ile mümkündür. Maruz kaldığı yükler göz önünde bulundurulduğunda yüzer rüzgâr türbinleri tasarımı için kapsamlı yapısal analizlerin yapılması gerekir.

Yüzer rüzgâr türbinlerinin tasarımında yapının rüzgâr ve dalga tahrik kuvvetlerine tepkisinin belirlenmesi esastır. Yapının hareketleri tahrik kuvvetlerinde değişime sebep olurken, tahrik kuvvetleri de yapının hareketlerini etkiler. Bu ilişki yapının elastik hareketlerinin aerodinamik ve hidrodinamik yükler ile bağlı analizini, diğer bir deyişle aero-hidro-elastik analizinin yapılmasını gerektirir.

Bu çalışmada, rüzgâr türbinlerine yüzer destek yapısı olarak düşünülen büyük ölçekli bir platform, birbirleriyle aerodinamik etkileşimi ihmal edilen iki adet rüzgâr türbinini taşıyacak şekilde tasarlanmış ve yapının dalga ve rüzgâr yükleri altındaki aero-hidro-elastik yanıtı belirlenmiştir. Yüzer rüzgâr türbinlerinin dinamik analizi esnasında platformun yalnızca rijit hareketlerinin incelenmesinin yeterli olacağı genel olarak kabul görmüş olmasına rağmen, bu çalışmada, platformun boyutlarından dolayı elastik hareketler de dikkate alınmıştır.

Analiz çerçevesinde yapıya etkiyen rüzgâr hızlarının yükseklikle beraber artışı, bir başka deyişle hava akışındaki sınır tabaka etkisi, üstel fonksiyon yaklaşımı ile belirlenmiştir. Dalgaların modellenmesinde ise düzenli bir dalga için akışkan hareketini tanımlayan lineer dalga teorisi kullanılmıştır. Karışık deniz modellerine temel oluşturan bu teori dalga yüksekliğinin, dalga boyuna göre küçük olduğu kabulüne dayanır.

Platformun dinamik analizi için, öncelikle, tahrik kuvvetlerinden doğan yapısal tepkinin şekil değiştirme modları cinsinden temsil edilebileceği göz önüne alınarak, sonlu elemanlar yöntemi ile platformun dinamik karakteristikleri belirlenmiştir. Dinamik karakteristikler elde edilirken, türbinin pervane-motor beşiği düzeneği rotasyonel eylemsizliğe sahip noktasal kütle olarak düşünülmüş ve bu düzeneğin kule merkez hattı etrafındaki dönme serbestlik derecesinden dolayı, dinamik karakteristikler her bir vaka için rüzgâr geliş açısı dikkate alınarak güncellenmiştir.

Hidrodinamik kuvvetler, akışkan-yapı etkileşim kuvvetleri ve dalga tahrik kuvvetleri olarak ikiye ayrılır. Etkileşim kuvvetleri, yapının sakin sudaki hareketinden dolayı

ortaya çıkan akışkan kuvvetleridir. Dalga tahrik kuvvetleri ise yapının hareketsiz kabul edildiği bir durumda gelen dalgaların oluşturacağı kuvvetlerdir. Etkileşim kuvvetleri, yapının hareketi ile etrafa dağılan dalgaların hareketini tanımlayan radyasyon hız potansiyelinin, yapının dinamik karakteristiği olan mod şekilleri ile eşleştirilmesiyle yapının her bir doğal modu için elde edilebilir. Modal açılım olarak bilinen bu yaklaşım ile radyasyon potansiyelini tanımlayan sınır değer problemi akışkan-yapı ara yüzü üzerinde bir sınır integral denklem olarak ifade elde edilebilir. Bu integral denklem sınır eleman yöntemiyle çözülerek, yapı ıslak yüzeyi üzerindeki potansiyel dağılımı ve sonrasında yapıya etkiyen genelleştirilmiş etkileşim kuvvetleri (ek su kütlesi ve hidrodinamik sönüm etkileri olarak) elde edilmiştir. Sınır eleman uygulamasında kullanılan serbest yüzey Green fonksiyonunun akışkan serbest yüzey şartını tüm serbest yüzey üzerinde sağlamasından dolayı ortaya çıkan düzensiz frekans etkilerini ortadan kaldırmak için, yapının su hattındaki varsayımsal iç serbest yüzey, üzerinde duvar şartı tanımlanarak, problem sınır yüzeyine eklenmiştir. Genelleştirilmiş dalga tahrik kuvvetleri, gelen ve saçılan dalgaların hız potansiyelini içeren difraksiyon bir hız potansiyeliyle verilebilir. Bu çalışmada dalga tahrik kuvvetleri, Haskind ilişkileri kullanılarak, gelen dalga ve radyasyon potansiyelleri cinsinden doğrudan hesaplanmıştır. Akışkan-yapı etkileşim kuvvetlerinin zaman bölgesine taşınması, frekans bölgesi değerlerinin sayısal integrasyonu ile elde edilen etki-tepki fonksiyonlarına (impulse response function) konvolüsyon uygulanmasıyla gerçekleştirilmiştir. Bu ifade, belirli bir an için etkileşim kuvvetlerinin yapının hareket geçmişine bağlı olduğuna işaret eder. Bu nedenle, analiz esnasında yapının hareket geçmişinin belirli bir zaman dilimi için elde tutulması gerekir. Dalga tahrik kuvvetlerinin zaman bölgesinde temsili için, frekans bölgesinde birim dalga genliği için elde edilen tahrik kuvvetlerine sinüs dönüşümü uygulanmıştır. Dalga genlikleri Pierson-Moskowitz dalga spektrumu kullanılarak hesaplanmıştır.

Aerodinamik kuvvetler kanat eleman momentum teorisi kullanarak hesaplanmıştır. Bu teoride, rüzgâr türbini kanatları yeter sayıda elemanla ayrıklaştırılarak, her eleman kesiti üzerinde iki boyutlu akış analizi yapılır ve her eleman için elde edilen kuvvetler kanat boyunca tümlenerek rotor üzerindeki rüzgâr kuvvetleri elde edilir. Bu kapsamda, her zaman adımında rotor üzerindeki kuvvetler hesaplanmış ve motor beşiği aracılığıyla kulelere aktarılmıştır. Bu aşamada, açık kaynak simülasyon kodu FAST kullanılmıştır.

Sonlu eleman modeline türbin kulesinin üst noktasından aktarılacak aerodinamik yükler hesaplanırken, kanatların elastik hareketleri, jeneratörün dönme hareketi, şaft burulması ve motor beşiğinin yalpa hareketi dikkate alınmıştır. Aerodinamik kuvvetler laminer sabit hızlı rüzgâr durumu düşünülerek hesaplanmıştır.

Yapının zaman bölgesindeki genelleştirilmiş hareket denklemi durum uzayında temsil edilmiş, çözüm için 4. dereceden Runge-Kutta metodu kullanılmıştır. Her zaman adımı için yapı üzerine etkiyen tahrik ve etkileşim kuvvetleri ve bu kuvvetlere yapının cevabı olarak, deplasman, hız ve ivme değerleri elde edilmiştir.

Analizler sonucunda pervane-motor beşiği düzeneğinin yönünün dinamik karakteristikler üzerindeki etkisi gözlemlenmiş, modellenen rüzgâr türbininde bu düzenek kule ekseni etrafında dönme serbestlik derecesine sahip ise, her çevresel durum için dinamik karakteristiklerin güncellenmesi gerektiği sonucuna ulaşılmıştır.

İncelenen yüzer rüzgâr tribünü sistemi için, genelleştirilmiş aerodinamik kuvvetlerin genelleştirilmiş hidrodinamik kuvvetlere göre daha büyük mertebede olduğu gözlenmiştir. Yapısal tepkinin daha ziyade aerodinamik kuvvetlerce belirlenmesi,

etkileşim kuvvetleri şiddetinde kanat geçiş frekansı ile (üç kanatlı pervane için dönme frekansının üç katı) bir salınıma sebep olmuştur. İncelenen çevre durumları kapsamında, yapısal tepkinin yanal dalga-rüzgâr durumu için minimumda olduğu görülse de, azami enerji üretimi çaprazdan gelen dalga-rüzgâr durumu için elde edilmiştir.

1. INTRODUCTION

In recent years, the wind energy come into prominence as an alternative source of energy. Wind energy is predicted as one of the most capable renewable energy solution of the future. The estimated potential of wind power over the sites having wind speed more than 6.9 m/s at height 80 m is 72 TW for the year 2000, which is the approximately eight times of the world's energy needs [1]. However, the wind energy reveals many practical obstacles such as initial investment cost and technological immaturity. In this manner, many studies have been carried out to construct viable wind power plant by reducing the cost, in order to make use of this abundant energy source cost-effectively.

The installed wind energy power plants are of either onshore or offshore type. Numerous offshore wind energy plants have been constructed recently and more are on the way. According to European Wind Energy Association (EWEA), the offshore wind capacity are estimated to reach 40 GW by 2020 and 150 GW by 2030 in Europe [2]. The more power capturing capacity due to the lesser turbulence in wind and higher average wind speed along with the available area for construction at offshore site makes offshore plants more popular compared to the land based plants. Moreover, the visual and noise pollution are prevented by the offshore type plants that are far from
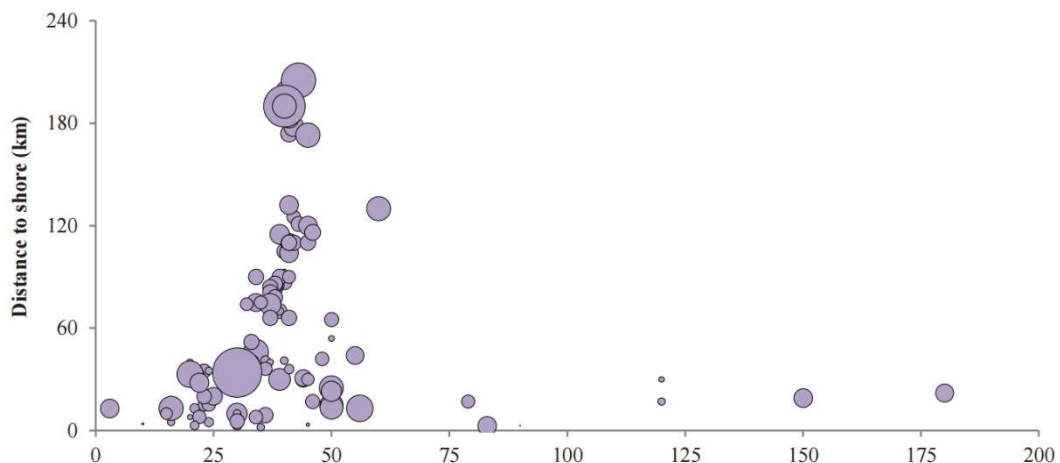
Figure 1.1 : Average water depth and distance to the shore of planned offshore wind projects [2].

1

the living space so that the project sites are expected to cover further sites from the shore. Figure 1.1 presents average water depth and distance to the shore of the planned offshore wind projects [3].

1.1 Floating Offshore Wind Turbines

Most of the offshore wind projects in operation were installed at nearshore as bottom founded wind turbines, since they are cost-effective at water depth less than 50 m. Deep water wind resources, however, are extremely abundant so that project sites are required to enlarge to far from shore [4]. For sites of depth more than 50 m, bottom founded type wind turbines are not economically feasible and planting floating type wind turbines become the norm [5].

Floating offshore wind turbines (FOWT) can carry larger wind turbines, accordingly, are capable of producing more energy with reduced final cost per MWh [2]. They can also substitute bottom founded wind turbines at soft seabed. However, the design of the FOWT brings inherent engineering challenges together. FOWT design should keep the motion of the system within acceptable limits and provide enough buoyancy to support the overall system weight. More dynamically coherent machinery design is needed as the turbine design is also impacted by the floater (platform) dynamics. For such systems, the design of the floater should be optimized, since the overall cost of depends mostly on the prices of the floater and power distribution system [6]. Extension of the installation site to deeper waters causes larger environmental loads, thereby; the response analysis of the floater is essential during the design phase and should consider both the wind and wave loads. Furthermore, interaction between floater hydrodynamics and rotor aerodynamics should be investigated [5].

The FOWTs may be divided into three main categories depending on the adopted strategy to establish the stability of the floating system.

1. Ballast: Stability is achieved via central buoyancy tank that provides high inertial resistance to roll and pitch motions.

2. Mooring Lines: Stability is achieved by the mooring line tension.

3. Buoyancy: Stability is achieved by water plane area of the floater.

2
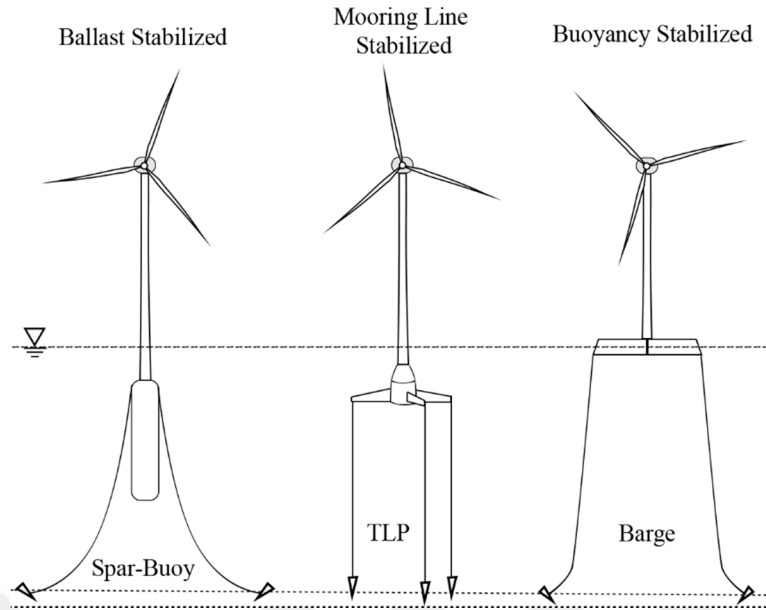
Figure 1.2 : Floating offshore wind turbine concepts.

The spar-buoy, tension leg platform (TLP), and barge type FOWT, given in Figure 1.2, are examples of ballast, mooring line, and buoyancy stabilized systems, respectively. Although the floating concepts are usually categorized based on the dominant source of stability, they are actually hybrid designs, ensuring the stability by employing each of the aforementioned methods [6].

A great number of studies is carried out to determine optimum floater design of the FOWT with respect to functionality and reduced cost. There are various possible floater configurations in design consideration either single-turbine or multi-turbine floater. The support structures of the multi-turbine floater can be classified as very large floating structure (VLFS) as the minimum distance between the turbines is limited due to the aerodynamic interactions between them. Some of the multi-turbine floater concepts are shown in Figure 1.3.
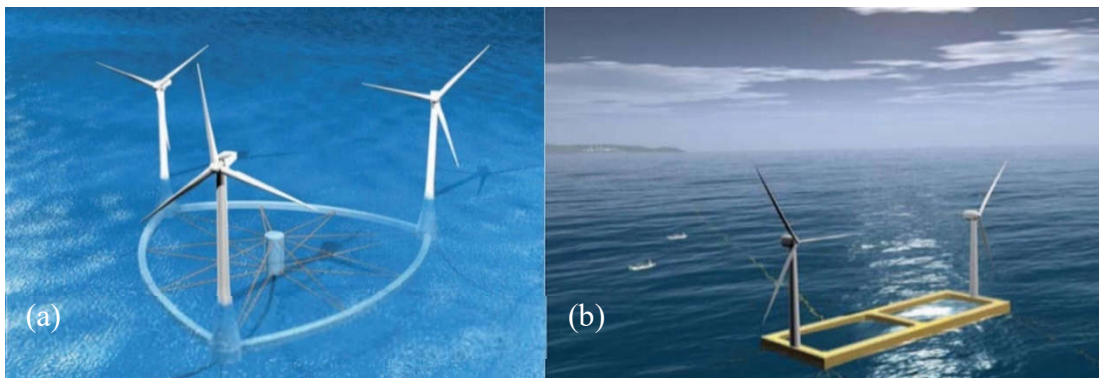
Figure 1.3 : (a) Semi-submersible type multi-turbine floater [7], (b) National Maritime Research Institute (NMRI) concept of ponton-type multi-turbine floater [5].

1.2 Very Large Floating Structures

Very large floating structures (VLFSs) can be thought of as man-made islands that enable ocean colonization. They may serve as a floating airport, bridge, pier, storage facility, industrial space, mobile offshore structure, entertainment facility, power plant and even as a floating city. Even though the VLFSs are mostly suggested as an alternative to land reclamation, technological developments permit the installation of these structures also at deep waters [8, 9]. They are cost-effective at deeper waters compared to classical land reclamation, nature-friendly, and easily constructed, transported and expanded. Moreover, they are isolated from seismic shocks [10].

VLFSs are principally structures having too large horizontal dimensions relative to its vertical dimension. In fact, VLFSs are identified by not only their larger horizontal dimension but also by having greater length than their characteristic length, defined by the ratio of the structural stiffness to the hydrostatic stiffness. The elastic responses of VLFSs, hence, become more dominant than their rigid-body responses [11]. Therefore, during the design of a VLFS, performing a dynamic fluid-structure interaction analysis with considering the elasticity of the structure, i.e., a hydroelastic analysis is essential.

VLFSs are generally divided into two categories, as pontoon-type and semi-submersible type. Pontoon-type VLFSs are suitable in calm water as they are more sensitive to wave excitation. Pontoon-type VLFSs are mostly erected at sheltered coastal formation and supported with breakwater to reduce the incident wave height. Mega-float in Tokyo Bay serving as an airport on the left in Figure 1.4 is a pontoon-type VLFS example. In open seas, semi-submersible type VLFSs are preferred in order

Mega-Float in Tokyo Bay   Aquapolis in Okinawa

Figure 1.4 : Pontoon-type VLFS and semi-submersible-type VLFS [10].

to sustain constant buoyancy and minimize the influences due to wave excitation [8].

On the right in Figure 1.4 a semi-submersible type VLFS, constructed in Okinawa in Japan, is shown.

1.3 Wind Turbine Components and Terminology

A wind turbine primarily consists of a rotor composed of blade, hub, nacelle, tower, and support structure as shown in Figure 1.5. The latter is a floater with mooring lines in case of floating systems. The plane area shaded by the rotor blades are known as the actuator disk. The nacelle encloses the wind turbine equipment, involving mainly
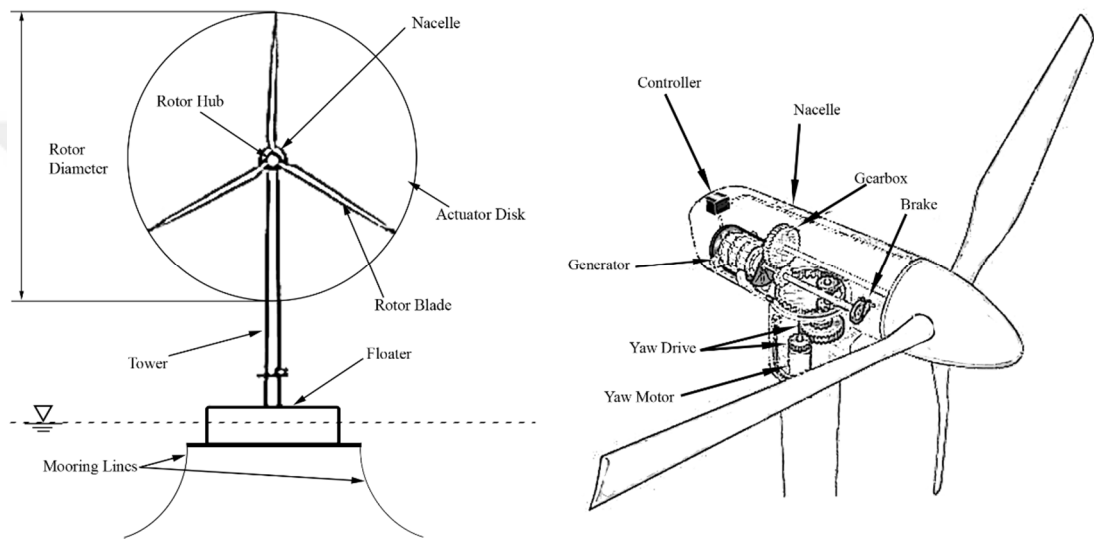
Figure 1.5 : Main components of floating offshore wind turbines and rotor-nacelle assembly (RNA).

gearbox, generator, control mechanism, and possibly yaw drivers. The rotor-nacelle assembly (RNA), seen on the right in Figure 1.5, is composed of everything beared by the tower. The parts of the turbine necessary to produce electricity, including the gearbox, generator, shafts, etc., are known as drivetrain.

The wind turbines have two possible configurations namely upwind and downwind, regarding how the wind encounters with the rotor, as seen in Figure 1.6. The blades passing in front of the tower of the downwind configuration is subjected to the tower shadow, which disrupts the wind flow and reduces the captured power. Most of the wind turbines, however, were constructed as upwind.

There are distinct degrees of freedom (DOFs) associated with the wind turbine components, which are identified by specific names. The definitions are given with respect to either rotating or non-rotating local coordinate systems. The blade
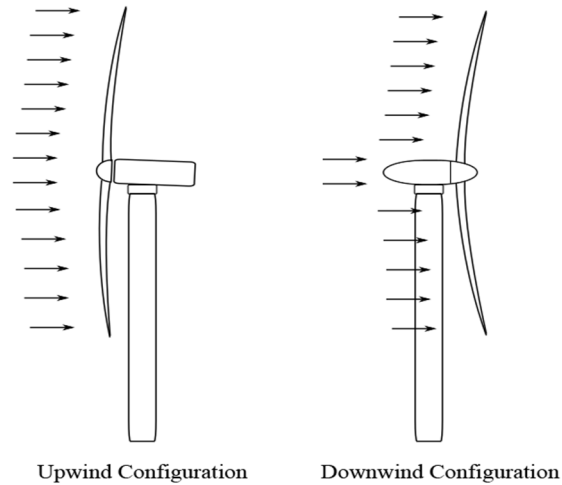
Figure 1.6 : Upwind and downwind wind turbine.

coordinate system is fixed at the blade root with its z-axis pointing toward the blade tip. The tower top and tower base coordinate systems are also fixed at the top and at the base of the tower. Their x, y-, and z-axes are longitudinal, lateral and upward direction, respectively. The hub coordinate system rotates with the rotor whereas the nacelle/yaw coordinate system rotates around the tower centerline with nacelle yaw.

The azimuth refers to the rotation of the rotor around the shaft axis, i.e., the rotation of the hub coordinate system, while blade pitch refers to the rotation of the blades around the z-axis of the blade coordinate system. Yaw denotes the rotation of the nacelle
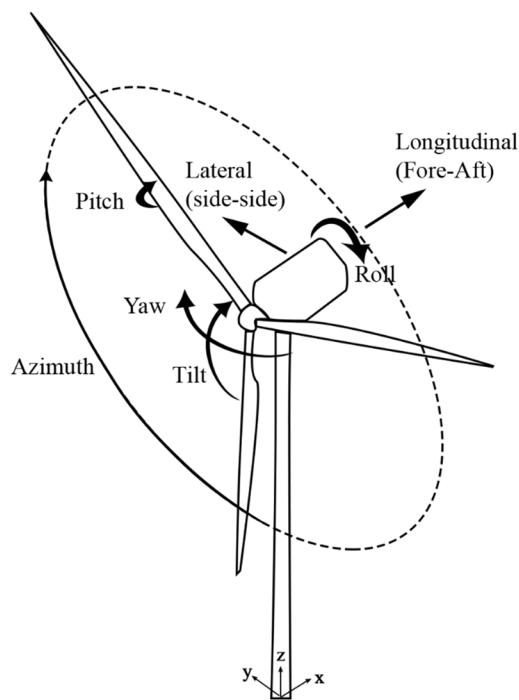
Figure 1.7 : Degrees of freedom of a wind turbine.

6

around the tower centerline. The motion of the rotor around the global *y*-axis is known as tilt motion. The flexible blade DOFs are named as flapwise and edgewise, representing the out-of-plane and in-plane bending, respectively. The flexible tower DOFs are known as side-to-side and fore-aft bending. All of these DOFs are illustrated in Figure 1.7.

1.4 Literature Review

The standard hydroelastic analysis approach for floating structures can be attributed to Bishop and Price [12]; the dry dynamic characteristics of the structure forms the basis of the analysis, where the small amplitude general frequency dependent response is represented by modal expansion in terms of natural modes. Here, the linear potential theory is adopted for the fluid motion.

Wu et al. [13] analyzed the hydroelastic response of a floating plate by using the eigenfunction expansion method. They applied an analytical approach to obtain the plate mode shapes and corresponding fluid velocity potential components. They considered both the rigid body and elastic motions and compared the predictions with the experimental results.

Huang and Riggs [14] developed an explicit formulation to determine the complete hydrostatic stiffness for the flexible structures by considering the internal stresses of the structure along with the external hydrostatic pressure. The structure is assumed at rest in calm water. The proposed method produces symmetric hydrostatic stiffness coefficients.

Ertekin et al [15] adopted the Haskind relation to compute the wave exciting forces in terms of incident and radiation velocity potentials and proposed the schemes of direct and modal approaches for coupling of the structural and fluid motion problems.

Lee at al [16] developed a numerical technique for the wave-structure interaction problems to remove the irregular frequency effects inherent to the boundary element solutions, when the free surface Green function is adopted as the fundamental solution. They extended the solution domain by appending the inner free surface, over which the rigid wall condition is applied.

Watanabe et al. [17] presented an approximate benchmark study for the hydroelastic analysis of a circular pontoon-type VLFS subjected to regular waves. They adopted the Mindlin plate model and Rayleigh-Ritz method for the solution.

Kara [18] developed a time domain numerical hydroelastic code to predict the hydroelastic response of floating bodies with zero and forward speed by computing the time domain radiation and wave excitation forces via the convolution of their impulse response functions. The method is verified by existing experimental results.

Thanks to the studies revealed the potential of offshore wind energy, FOWTs become an active research topic lately. Different types of FOWT floater designs are presented and investigated in terms of survivability, reliability, and availability. Wang et al. [5] presented a review for floater conceptual designs.

Musial et al. [4] conducted a feasibility study on several FOWT types. They categorized the floaters mainly as multi-turbine and single-turbine. A financial comparison between two single-turbine floaters with different mooring systems is also presented.

Butterfield et al [19] analyzed the design challenges for certain floater types by classifying the floaters according to the static stability criteria. Prescribed challenges are assessed for each floater type by considering the financial conditions.

Jonkman [20] developed a hydrodynamic analysis tool, in addition to the time domain simulation tool FAST presented by National Renewable Energy Laboratory (NREL), to analyze the coupled dynamic response of the FOWTs and performed a load analysis for one of the floater concepts. Here, the impulse response function (IRF) is employed to derive the wave forces in time domain.

Matha [21] performed an extensive load and stability analysis of a TLP type FOWT by using the time domain aero-hydro-servo-elastic design code FAST with AeroDyn and HydroDyn. A comparison of instability and fatigue lifetime prediction between TLP, spar-buoy, and land-based wind turbine systems is presented.

Ramachandran et al. [22] compared the RAOs obtained from different analysis tools. They initially assumed the wind turbine as rigid and non-operating, i.e. not subjected to wind excitation, and then extended the analysis by considering the structural flexibility of blades and tower, aerodynamic damping, and control mechanism. The

effects of the aerodynamic damping and gyroscopic excitation due to the rotating rotor on the dynamic response are also presented.

Ma et al. [23] have developed a numerical simulation method to analyze coupled FOWT and mooring systems by considering the flexibility of the floater and nonlinearity of the mooring line. They also carried out a series of experiment of the scaled FOWT model under the excitation of steady wind and regular waves to validate the numerical method.

Iijima et al. [24] proposed a numerical procedure to perform a coupled time-domain aerodynamic and hydrodynamic analysis for the pontoon-type multi-turbine floaters developed at NMRI (see Figure 1.3b). Here, the flexibility of both support structures, including the tower and blades, and wave and wind excitation forces are taken into account, though the interaction between the rotors is ignored.

Within the scope of this thesis, the time domain response analysis of a large-scale support structure carrying two 5MW wind turbines, which is classified as VLFS due to its dimension, is performed under combined wave and wind loads. The dynamic characteristics of the structure, i.e., natural frequencies and mode shapes, are obtained using the finite element method (FEM) in order to represent the structural response, which is described by the modal approach. The fluid perturbation due to structural motion—given in terms of potential distributions and represented similarly by modal expansion—is related with the response through the kinematical boundary condition. The hydrodynamic forces on the structure are computed by applying the Boundary Element Method (BEM) in the frequency domain. The resulting frequency dependent wave radiation (in other words, fluid-structure interaction) forces and wave excitation forces are transformed into their time domain representation. The time domain interaction forces are calculated by the convolution of the impulse response functions that are obtained from the radiation forces. The time domain representation of the excitation forces for the irregular incident waves is obtained by the Fourier transformation of the wave exciting forces corresponding to the unit wave amplitude. Here, the Pierson-Moskowitz wave spectrum is applied for the specified wind velocity. The aerodynamic forces on the rotor are obtained by the Blade Element Momentum Theory (BEMt). The time integration of the structural responses are computed by forming the state-space model.

2. MATHEMATICAL MODEL

2.1 Introduction

A time domain aero-hydro-elastic solution procedure is formed to investigate the elastic response of the multi-rotor floating wind turbine structure under combined wind and wave loads. The aerodynamics of the rotor is calculated by considering the steady wind flow with laminar boundary layer effects and using the Blade Element Momentum Theory (BEMt). On the other side, the wave kinematics is determined by using the linear wave theory and adopting the irregular sea state. The corresponding hydrodynamics interaction and wave forces in terms of potential distribution over the wetted surface of the floater is computed by using the Boundary Element Method (BEM). In order to obtain the time domain response of the structure, including the tower and floater, the state-space formulation of the generalized equation of motion is solved by applying a time integration scheme. The response is determined under several conditions of the combined wave-wind loads.

The BEMt is based on the spanwise integration of the forces calculated by the 2D flow analysis at each blade cross section. Accordingly, the obtained forces are then transmitted to the structure through the components of the nacelle at each time step.

The modal expansion methodology, which can efficiently couple the structural deformation with the fluid perturbation, is employed to establish the wave-structure interaction problem in the frequency domain. The method estimates the structural response as the superposition of natural (dry) modes, where the series coefficients, so called principle coordinates, describe the contribution of individual modes within the overall response. Fluid velocity potential is also decomposed into components corresponding to each considered mode shape, and the response and potential components are related through the kinematical boundary condition. The wave excitation forces for the unit amplitude regular waves are determined by using the Haskind relation. The fluid-structure interaction (radiation) forces and wave excitation

forces obtained in the frequency domain in generalized forms are transformed into the time domain as impulse response functions (IRFs) by using the Fourier transformation.

In order to derive the external loading on the structure, the environmental conditions should be defined. First, the wind and wave characteristics and their mathematical approximation are introduced. Then, the numerical procedure to obtain the frequency dependent interaction and exciting forces and their time domain transformation are presented. Finally, the response of the floater under combined wave and wind loads is obtained by solving the generalized equations of motion.

2.2 Wind Characteristics

The wind environment can be represented by selecting an appropriate wind model depending on the circumstances. Assuming that the wind is steady, homogenous, uniform and unidirectional, as shown in Figure 2.1a, its aerodynamic can be efficiently studied. The airflow where the turbines are located, however, is subjected to boundary layer effect due to the viscosity and no-slip condition at the earth surface. Thus, the flow velocity in boundary layer decreases with elevation. This is determined by the uniform wind shear model illustrated in Figure 2.1b. In fact, inherently rough surface of the earth causes inhomogeneous, unsteady and turbulent flow. The turbulent wind model, demonstrated in Figure 2.1c, involves the sudden fluctuation in velocity and pressure [25].

Wind shear model is approximated by either power law profile or logarithmic wind profile. The power law describing the relation between height and wind speed is given as follow,
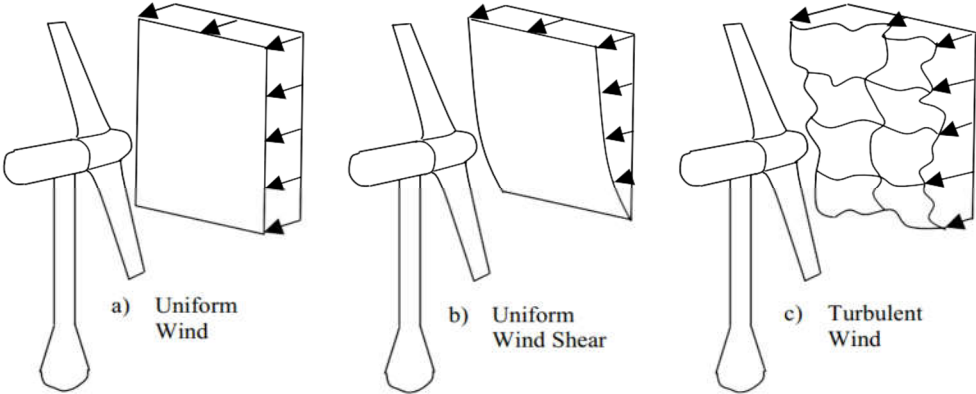
Figure 2.1 : Wind Characteristics [25].

$$\frac{U_2}{U_1} = \left(\frac{z_2}{z_1}\right)^{\alpha} \tag{2.1}$$

where U_1 and U_2 are the wind speeds at heights z_1 and z_2, while α stands for the wind shear exponent.

On the other side, logarithmic wind profile relates the wind speed with the elevation as,

$$\frac{U_2}{U_1} = \frac{\ln(z_2 / z_r)}{\ln(z_1 / z_r)}. \tag{2.2}$$

Here, z_r is the roughness length, where mean speed is assumed zero [26].

2.3 Linear Wave Theory

Linear wave theory is the most basic mathematical model to represent the regular water waves. The theory, however, is often preferred for engineering problems, since it provides accurate approximation and representation of the irregular waves in terms of regular waves.

If the length of the structure along the waves is greater than about one-fifth of the wavelength, effects of the flow separation and friction drag can be neglected, so that the flow can be assumed inviscid. Furthermore, the water is essentially incompressible. The continuity equation for the incompressible and homogenous fluid may be expressed as,

$$\nabla.\mathbf{v}(\mathbf{x},t) = 0 \tag{2.3}$$

where $\mathbf{v}$ is the velocity vector, $\mathbf{x} = (x, y, z)^{\mathrm{T}}$ and t denote the position vector and time, respectively. Assumption of the irrotational fluid motion leads to the equation

Assumption of the irrotational fluid motion leads to the equation

$$\nabla \mathrm{x} \mathbf{v}(\mathbf{x},t) = 0 \tag{2.4}$$

which is satisfied if the fluid velocity vector is given as the gradient of the velocity potential $\Phi(\mathbf{x},t)$.

$$\mathbf{v}(\mathbf{x},t) = \nabla\Phi(\mathbf{x},t) \tag{2.5}$$

Therefore, the motion of the fluid could be expressed in terms of a velocity potential function by the Eq. (2.3) and (2.5) satisfying Laplace's equation throughout the fluid domain Ω,

$$\nabla^2 \Phi = 0 \ in \ \Omega \tag{2.6}$$

Water waves can be defined by the deformation of the free surface. The fluid particles excited by the propagating waves are assumed not to propagate with the waveform. The characteristics of the water waves are demonstrated in Figure 2.2.

The fluid motion at the free surface satisfies the dynamic and the kinematic boundary conditions. In linear wave theory, it is assumed that the wave height is much smaller than the wavelength. Hence, the dynamic boundary condition stating the equality of the fluid pressure to the atmospheric pressure on the free surface may be expressed in the following linear form by neglecting the second order terms in Bernoulli's equation.

$$\zeta = -\frac{1}{g}\frac{\partial \Phi}{\partial t} \quad on \quad S_f \tag{2.7}$$

Here, S_f and ζ denote the free surface and free surface elevation, respectively, and g is the gravitational acceleration. The accompanying kinematic boundary condition states that the fluid particles on the free surface follow the vertical motions of the wave profile,

$$\frac{\partial \Phi}{\partial z} = \frac{\partial \zeta}{\partial t} \quad on \quad S_f \tag{2.8}$$

where, z is vertical axis with the positive direction upwards.

Combining Eqs. (2.7) and (2.8), the linear free surface boundary condition is obtained,
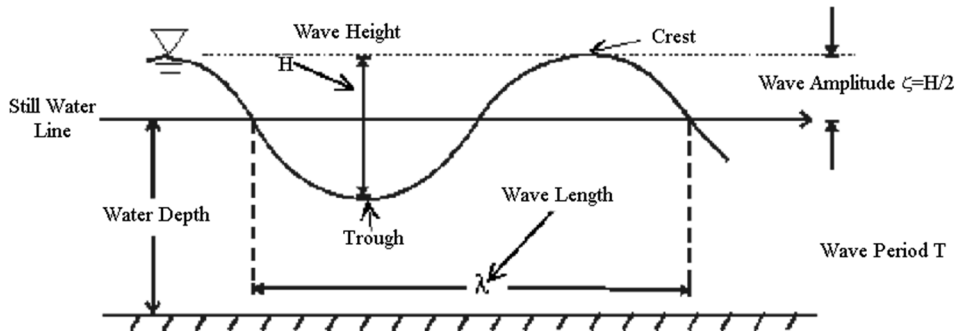
Figure 2.2 : Wave propagation [27].

14

$$g\frac{\partial \Phi}{\partial z} + \frac{\partial^2 \Phi}{\partial t^2} = 0 \quad \text{on} \quad S_f \tag{2.9}$$

At the sea bottom, there is no flow in normal direction. Considering the horizontal flat bottom, the seabed kinematic boundary condition can be written as,

$$\frac{\partial \Phi}{\partial z} = 0 \quad \text{on } z = -h \tag{2.10}$$

In the absence of the body, the velocity potential for a progressive wave satisfying the boundary conditions (2.9) and (2.10) can be given as [7],

$$\Phi_I(\mathbf{x},t) = \text{Re}\left\{\frac{ig\zeta}{\omega}\frac{\cosh k(z+h)}{\cosh kh}e^{i[k(x\cos\alpha + y\sin\alpha)+\omega t]}\right\} \tag{2.11}$$

Here, ω and ζ are the frequency and amplitude of the propagating waves in a water of uniform depth h, respectively, α is the incident angle, as shown in Fig. 1.2, and k is the wave number given by the dispersion relation

$$\omega^2 = gk\tanh kh. \tag{2.12}$$

In deep water, $\tanh kh$ approaches one and the dispersion relation for the deep water is given as

$$k = \omega^2/g \tag{2.13}$$

Subsequently, the incident wave potential of deep water can be given from Eq. (2.11) as [28],

$$\Phi_I(\mathbf{x},t) = \frac{g\zeta}{\omega}e^{kz}e^{i[k(x\cos\alpha + y\sin\alpha)+\omega t]} \tag{2.14}$$

Figure 2.3 : Definition of incident wave angle.

2.4 Generalized Equation of Motion

The dynamic response of a structure due to external forces can be described by the discretized equation of motion,

$$\mathbf{M}\ddot{\mathbf{q}}(t) + \mathbf{C}_V\dot{\mathbf{q}}(t) + \mathbf{K}\mathbf{q}(t) = \mathbf{F}(t), \tag{2.15}$$

where $\mathbf{M, C, K}$ represent the mass, structural damping and stiffness matrices, $\mathbf{q}, \dot{\mathbf{q}}$ and $\ddot{\mathbf{q}}$ stands for the time-dependent displacements, vel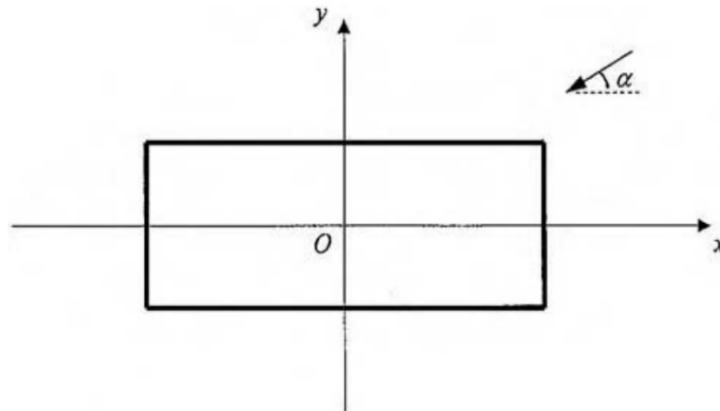ocities and accelerations respectively, $\mathbf{F}$ is the vector denoting the external forces and t represents the time. The displacement vector can be expressed as

$$\mathbf{q}^{\mathrm{T}} = [\mathbf{q}_1\,\mathbf{q}_2\dots\mathbf{q}_j\dots\mathbf{q}_n], \tag{2.16}$$

where n denotes the number of nodes and $\mathbf{q}_j$ represents the nodal displacement components with three translations u_x, u_y, u_z and three rotations θ_x, θ_y, θ_z. Thus, the displacement vector for each node can be written as,

$$\mathbf{q}_j^{\mathrm{T}} = [u_x\,u_y\,u_z\,\theta_x\,\theta_y\,\theta_z]_j. \tag{2.17}$$

For an undamped free vibration, in other words in vacuo analysis, the equation of motion of the structure becomes,

$$\mathbf{M}\ddot{\mathbf{q}}(t) + \mathbf{K}\mathbf{q}(t) = 0 \tag{2.18}$$

By substituting the solution $\mathbf{q} = \mathbf{u}e^{i\omega t}$, Eq. (2.18) can be written as

$$(-\omega^2\mathbf{M} + \mathbf{K})\mathbf{u} = 0 \tag{2.19}$$

Eq. (2.19) forms the eigenvalue problem, solution of which gives the dynamic characteristics, i.e., natural frequencies ω and corresponding mode shapes (normal modes) $\mathbf{u}$ of the structure.

The general forced response of a structure may be expanded with a set of appropriate normal modes in following form,

$$\mathbf{q}(t) = \sum_{i=1}^{n_m}\mathbf{u}_i p_i(t) = \mathbf{U}\mathbf{p}(t) \tag{2.20}$$

where the modal matrix $\mathbf{U}$ consists of the normal mode vectors $\mathbf{u}_i$, and $\mathbf{p}(t)$ is the principle coordinates vector standing for the deflection components in the n_m-

dimensional modal vector space, where n_m indicates the number of considered principal modes. Eq. (2.15) may be written in terms of principal coordinates $\mathbf{p}(t)$ by using Eq. (2.20) and pre-multiplying by $\mathbf{U}^T$

$$\mathbf{a}\ddot{\mathbf{p}}(t) + \mathbf{b}\dot{\mathbf{p}}(t) + \mathbf{c}\mathbf{p}(t) = \mathbf{f}(t) \qquad \textbf{(2.21)}$$

Here, $\mathbf{a, b}$ and $\mathbf{c}$ stand for the generalized matrices of mass, damping and stiffness, respectively, and given as

$$\mathbf{a} = \mathbf{U}^T\mathbf{M}\mathbf{U}, \ \mathbf{b} = \mathbf{U}^T\mathbf{C}_V\mathbf{U}, \ \mathbf{c} = \mathbf{U}^T\mathbf{K}\mathbf{U}, \ \mathbf{f}(t) = \mathbf{U}^T\mathbf{F}(t) \qquad \textbf{(2.22)}$$

The generalized mass and stiffness matrices are diagonal; however, the damping matrix does not have to be diagonal. The generalized external force vector $\mathbf{f}(t)$ that represents the fluid-structure interaction and all other external forces can be expressed as [29],

$$\mathbf{f}(t) = -(\mathbf{A}\ddot{\mathbf{p}}(t) + \mathbf{B}\dot{\mathbf{p}}(t) + \mathbf{C}\mathbf{p}(t)) + \mathbf{\Xi}(t), \qquad \textbf{(2.23)}$$

where, $\mathbf{A, B}$ and $\mathbf{C}$ are the generalized added mass, fluid damping, and fluid stiffness matrices, respectively, and $\mathbf{\Xi}(t)$ denotes the generalized external force vector caused by wave, wind, mechanical excitation, etc.

The governing equation of motion in Eq. (2.21) then can be expressed as follows,

$$(\mathbf{a} + \mathbf{A})\ddot{\mathbf{p}}(t) + (\mathbf{b} + \mathbf{B})\dot{\mathbf{p}}(t) + (\mathbf{c} + \mathbf{C})\mathbf{p}(t) = \mathbf{\Xi}(t). \qquad \textbf{(2.24)}$$

2.5 Frequency Domain Hydrodynamics

2.5.1 The wave-structure interaction problem

The hydrodynamic loads on the body floating near the free surface are formulated by the wave diffraction and radiation potentials, which can be defined by the Laplace's equation. Total velocity potential can be expressed as the sum of radiation and diffraction potentials,

$$\Phi = \Phi_R + \Phi_D. \qquad \textbf{(2.25)}$$

The radiation potential represents the velocity potential in the absence of the incident waves. For instance, in calm water, if the body is forced to oscillate, the resulting fluid motion will be represented by the radiation potential. On the other hand, the diffraction potential arise from the presence of the incident waves and its interaction with floating

body. Under the assumptions of the linear theory, this potential may be defined about the fixed body, independent of its motions [28].

The diffraction potential may be further decomposed as

$$\Phi_D = \Phi_I + \Phi_S, \tag{2.26}$$

where Φ_I is the incident wave potential, given by Eq. (2.14) for deep water, and Φ_S is the scattering wave potential representing the disturbance of the incident waves by the presence of the body. The diffraction potential satisfies the following boundary condition on the wetted surface of the body,

$$\partial \Phi_D / \partial \mathbf{n} = \partial \Phi_S / \partial \mathbf{n} + \partial \Phi_I / \partial \mathbf{n} = 0, \ \ \text{on} \ S_w \tag{2.27}$$

Here, $\mathbf{n}$ is the unit normal vector on the wetted surface of the structure, S_w, pointing out of the fluid domain.

A modal expansion similar to Eq. (2.20) can be adopted for the radiation potential, by proposing a series of potential components corresponding to each principal coordinate used in Eq. (2.20). Thus, the radiation potential in Eq. (2.25) can be rewritten as follows,

$$\Phi_R(\mathbf{x}, t) = \sum_{i=1}^{n_m} \Phi_i(\mathbf{x}) p_i(t), \tag{2.28}$$

$$p_i(t) = p_i e^{i\omega t}. \tag{2.29}$$

where, Φ_i and $p_i(t)$ refer to the spatial distribution of the radiation potential and the principle coordinate associated with the ith principal mode, respectively. n_m is the number of considered modes in the dry analysis.

The radiation potential is due to the structural motion, so a Neumann type boundary condition, stating the equality of the fluid and body normal velocities must be expressed over the fluid-structure interface. Using Eqs. (2.5), (2.20), and (2.28), the kinematical boundary condition for each potential component can be given as

$$\frac{\partial \Phi_i}{\partial \mathbf{n}} = \frac{\partial}{\partial t} \mathbf{u}_i, \ \text{on} \ S_w \tag{2.30}$$

Eq. (2.30) relates potential components with the normal modes of the floating body.

Considering the time harmonic form of the motion, boundary conditions stated in Eq. (2.9), (2.10) and (2.30) can be rewritten as

$$\frac{\partial \Phi}{\partial z} = \frac{\omega^2}{g}\Phi \quad \text{on} \quad S_f \tag{2.31}$$

$$\frac{\partial \Phi}{\partial z} = 0 \quad \text{on} \quad z = -h \tag{2.32}$$

$$\frac{\partial \Phi_i}{\partial n} = i\omega \mathbf{u}_i \quad \text{on} \quad S_w \tag{2.33}$$

The waves on the free surface except due to the incident wave potential itself have to be radiating away from the body. For the infinite fluid domain, the additional condition stating that the effects of the body on fluid domain will diminish with the distance, r, from the source (so-called radiation condition) can be expressed as

$$\lim_{r \to \infty} \sqrt{r}\left[\frac{\partial(\Phi - \Phi_I)}{\partial r} + ik(\Phi - \Phi_I)\right] = 0. \tag{2.34}$$

2.5.2 The boundary element solution of the potential problem

In order to compute the interaction forces, the distribution of the velocity potential on the wetted surface should be determined. The potential problem defined by the Laplace equation and boundary conditions in Eqs. (2.31)-(2.34) can be expressed by the boundary integral equation (BIE) reducing the problem domain to the interface surface. The BIE can be determined through Green's identities [30], Betti's theorem [31] or weighted residual method [32] and solved by using the BEM.

By considering the potential functions ϕ and ψ, satisfying the Laplace equation in the domain Ω, the Green's second identity is stated as follow,

$$\int_{\Omega}(\psi \nabla^2 \phi - \phi \nabla^2 \psi)\mathrm{d}\Omega = \int_{\Gamma}\left(\psi \frac{\partial \phi}{\partial n} - \phi \frac{\partial \psi}{\partial n}\right)\mathrm{d}\Gamma \tag{2.35}$$

where, Γ is the boundary surface of the domain Ω. The solution of a differential equation for a unit point source in an infinite domain Ω_{∞} is entitled as the fundamental solution and defined as,

$$\mathcal{L}u^* = -\delta(\mathbf{x}, \boldsymbol{\xi}). \tag{2.36}$$

Here, u^* is the fundamental solution, $\mathcal{L}$ is the differential operator, and $\boldsymbol{\xi} = (\xi, \eta, \zeta)$ and $\mathbf{x}$ represents the source and field points in the domain, respectively. $\delta(\mathbf{x}, \boldsymbol{\xi})$ is the Dirac delta function given as,

$$\delta(\mathbf{x}, \boldsymbol{\xi}) = \begin{cases} 0 & \mathbf{x} \neq \boldsymbol{\xi} \\ \infty & \mathbf{x} = \boldsymbol{\xi} \end{cases} \qquad (2.37)$$

and it satisfies the following equations,

$$\int_{\Omega_\infty} f(\mathbf{x})\delta(\mathbf{x}, \boldsymbol{\xi}) d\Omega_\infty = f(\boldsymbol{\xi}) \qquad (2.38)$$

$$\int_{\Omega} f(\mathbf{x})\delta(\mathbf{x}, \boldsymbol{\xi}) d\Omega = \begin{cases} 0 & \boldsymbol{\xi} \notin \Omega, \Gamma \\ f(\boldsymbol{\xi}) & \boldsymbol{\xi} \in \Omega \\ \text{undefined} & \boldsymbol{\xi} \in \Gamma \end{cases} \qquad (2.39)$$

If the source point is on the surface Γ the integral becomes undefined. However, it can be calculated in the limit that the radius of the circular boundary approaches to zero. By replacing Ψ with the fundamental solution, defining the flux as $q = \partial\phi/\partial n$, and using Eqs. (2.36) and (2.39), Eq. (2.35) can be stated as follows [33],

$$\phi(\boldsymbol{\xi}) = \int_{\Gamma} \left(\phi^*(\mathbf{x}, \boldsymbol{\xi}) q(\mathbf{x}) - \phi(\mathbf{x}) q^*(\mathbf{x}, \boldsymbol{\xi}) \right) d\Gamma. \qquad (2.40)$$

Eq. (2.40), however, includes singularities since Eq. (2.39) is undefined on the surface Γ. These singularities, however, can be suppressed by defining a small circular boundary around the source point with radius ξ and calculating integrals while ξ approaches to the surface Γ. Then, Eq. (2.40) turns into the following BIE of the potential problem.

$$c(\boldsymbol{\xi})\phi(\boldsymbol{\xi}) + \int_{\Gamma} \phi(\mathbf{x}) q^*(\mathbf{x}, \boldsymbol{\xi}) \, d\Gamma = \int_{\Gamma} \phi^*(\mathbf{x}, \boldsymbol{\xi}) q(\mathbf{x}) d\Gamma \qquad (2.41)$$

Here, $c(\boldsymbol{\xi})$ is the free-term, resulting from the calculation of the singular integrals that identifies the fraction of $\phi(\boldsymbol{\xi})$ lying inside the domain of interest. The BIE can be applied to the free-surface problem by defining the fundamental solution satisfying the free surface and the radiation condition, i.e. free surface Green's function which is given as follows [34].

20

$$G = \frac{1}{4\pi}\left(\frac{1}{r} + \frac{1}{r'} + H\right) \tag{2.42}$$

Here, H represents the influences of the free surface in Green's function, while r and r' denote the distance between the source point and the field point and the free surface image of the source point and the field point, respectively.

$$r = \left[(\xi - x)^2 + (\eta - y)^2 + (\zeta - z)^2\right]^{1/2}$$
$$r' = \left[(\xi - x)^2 + (\eta - y)^2 + (\zeta + z)^2\right]^{1/2} \tag{2.43}$$

Since the Green's function satisfies all the boundary conditions except for the wetted surface, the BIE can be defined over the wetted surface of the structure S_w,

$$c(\xi)\phi(\xi) + \int_{S_w} \phi(\mathbf{x})G_{,n}(\mathbf{x}, \xi)\mathrm{d}S = \int_{S_w} G(\mathbf{x}, \xi)q(\mathbf{x})\mathrm{d}S \tag{2.44}$$

The general solution of Eq. (2.44) requires the discretization of the interface surface with boundary elements, so that the potential function and body normal velocity distributions over the interface can be approximated using shape functions and nodal potential and flux values. For the ith boundary element, the corresponding representations Φ^i and q^i can be given as

$$\phi^i = \sum_{j=1}^{e_i} N_j\phi_{ij} \quad , \quad q^i = \sum_{j=1}^{e_i} N_j q_{ij}. \tag{2.45}$$

Here, e_i is the number of nodal points assigned to the boundary element, ϕ_{ij} and q_{ij} respectively represent the potential and flux values for the jth nodal point of the element, and N_j denotes the associated shape function. The shape functions are used to represent the distribution of the potentials over the related element. The linear shape functions are given as follows,

$$N_1 = \left((1-\zeta)(1-\eta)\right)/4 \,,\, N_2 = \left((1+\zeta)(1-\eta)\right)/4$$
$$N_3 = \left((1+\zeta)(1+\eta)\right)/4 \,,\, N_4 = \left((1-\zeta)(1+\eta)\right)/4 \tag{2.46}$$

By taking the nodal points of the discretization as the source point and substituting Eq. (2.45) with the boundary condition (2.33) into Eq. (2.44), the following set of algebraic equations can be written in terms of nodal potential function and body normal velocity values:

$$c_k \phi_k + \sum_{i=1}^{n_e} \sum_{j=1}^{e_i} \phi_{ij} \int_{S_i} N_j G_{,n} dS = i\omega \sum_{i=1}^{n_e} \sum_{j=1}^{e_i} \mathbf{u}_{ij} \int_{S_i} N_j G dS , \quad k = 1, ..., n_n \tag{2.47}$$

Here, n_n and n_e are the numbers of nodal points and boundary elements, respectively, used in the discretization, S_i is the area of the ith boundary element, and ϕ_k represents the potential value for the kth nodal point. The resulting system of equations after completing the surface integrations in Eq. (2.47) can be given with the matrix form

$$\mathbf{H}\mathbf{\Phi} = i\omega \mathbf{G}\mathbf{q}. \tag{2.48}$$

2.5.3 Generalized hydrodynamic forces

Using the Bernoulli's equation by neglecting the second-order terms, the fluid pressure, $P(\mathbf{x}, t)$, on the floating body can be given as.

$$P(\mathbf{x}, t) = -\rho \left(\frac{\partial \Phi(\mathbf{x}, t)}{\partial t} + gz \right) \tag{2.49}$$

By substituting Eq. (2.28)-(2.29) into Eq. (2.25) the total velocity potential can be expressed as,

$$\Phi(\mathbf{x}, t) = \mathrm{Re} \left\{ \left(\sum_{j=1}^{n_m} \Phi_j p_j + \zeta(\Phi_I + \Phi_S) \right) e^{i\omega t} \right\} \tag{2.50}$$

where ζ is the incident wave amplitude. Using Eq. (2.50) for the velocity potential in Eq. (2.49), the pressure expression can be arranged as follows.

$$P = -\rho \mathrm{Re} \left\{ \left(\sum_{j=1}^{n_m} \Phi_j p_j + \zeta(\Phi_I + \Phi_S) \right) i\omega e^{i\omega t} \right\} - \rho gz \tag{2.51}$$

The hydrodynamic force on the body related with the jth mode shape can be expressed by integrating the fluid pressure over the wetted surface:

$$
\begin{aligned}
\mathbf{f}_{H_j}(t) = & -\rho g \iint_{S_w} z \, \mathbf{n} dS \\
& -\rho \mathrm{Re} \left\{ \sum_{j=1}^{n_m} i\omega p_j e^{i\omega t} \iint_{S_w} \Phi_j \, \mathbf{n} dS \right\} \\
& -\rho \mathrm{Re} \left\{ i\omega \zeta e^{i\omega t} \iint_{S_w} (\Phi_I + \Phi_S) \mathbf{n} dS \right\}.
\end{aligned}
\tag{2.52}
$$

The force components in Eq. (2.52) represent different aspects of the hydrodynamic problem. The first term is the hydrostatic component. The second term is due to radiation problem and can be associated with the *added-mass* and *hydrodynamic damping* effects through its real and imaginary parts, respectively. The last term is related with the diffraction problem representing the wave excitation forces, proportional to the incident wave amplitude.

2.5.3.1 Hydrostatics

The leading term in Eq. (2.52), representing the forces associated with the vertical displacement, is known as the hydrostatic restoring force. The restoring force is generally expressed in terms of hydrostatic stiffness coefficients. The hydrostatic stiffness associated with the rigid body motion is well known, however in hydroelasticity, this stiffness matrix has to be extended to cover also the elastic motions. Furthermore, the hydrostatic stiffness matrix should consider all displacement related variations of the forces such as internal forces [14].

When the hydrostatic stiffness of the flexible structure is formed, the structure can be assumed at rest in calm fluid, and subjected only to the gravity forces. The hydrostatic forces are divided into two components as external and internal forces. External forces result from the hydrostatic pressure on the wetted surface and the structural weight, whereas internal forces are due to the internal stresses [14]:

$$\mathbf{f}_{HS_i}^E = \int_{S_w} (\mathbf{n}.\mathbf{u}_i).\mathbf{p}\, dS - \rho_s g \int_{\Omega_s} (\mathbf{n}.\mathbf{u}_i)\, d\Omega \tag{2.53}$$

$$\mathbf{f}_{HS_i}^I = \int_{\Omega_s} \sigma_{kl} \varepsilon_{kl}^i\, d\Omega \tag{2.54}$$

Here, ρ_s is the mass density of the structure and Ω_s is the structural volume in the equilibrium configuration. σ_{kl} is the actual stress tensor and ε_{kl}^i is the strain tensor that is compatible with the normal mode $\mathbf{u}_i$. Thus, the hydrostatic stiffness matrix $\mathbf{C}$ presented in Eq. (2.24) can be expressed as,

$$\mathbf{C} = \mathbf{C}^h + \mathbf{C}^g \tag{2.55}$$

where $\mathbf{C}^h$ represents the hydrostatic stiffness due to the external forces and $\mathbf{C}^g$, known as the geometric stiffness matrix, results from the internal stresses.

The stiffness coefficients can be derived by a consistent linearization of the internal and external forces via the directional derivative [35],

$$C_{ij}^{h,g} = -\nabla \mathbf{f}_{HS_i}^{E,I} \mathbf{u}_j \tag{2.56}$$

where, superscript E and I indicate the external and internal forces. Substitution of Eq. (2.56) into Eq. (2.55) yields the explicit expression of the complete hydrostatic stiffness (see detailed derivation in Ref. [14]),

$$C_{ij} = -\rho g \int_{S_w} u_k^i (u_3^j + z \varepsilon_\upsilon^j) n_k dS + \rho g \int_{S_w} z u_l^i u_{k,l}^j n_k dS + \int_{\Omega_s} \sigma_{lm} u_{k,l}^i u_{k,m}^j d\Omega. \tag{2.57}$$

Here, $\varepsilon_\upsilon^j \equiv u_{l,l}^j$ is the volumetric strain and n_k is the kth member of unit normal vector.

Since the hydroelasticity of the floating structures are generally analyzed by adopting two-dimensional elements, the formulation can be specialized for a plate element by adopting the Kirchhoff plate model. The plate stiffness is formulated in a local coordinate system, $\bar{x} - \bar{y} - \bar{z}$, where $\bar{z}$ is normal to the plane surface. Assuming that either top or bottom surface parallel to the $\bar{x} - \bar{y}$ plane is subjected to the hydrostatic pressure, the other surface and the four edges are dry, considering the internal stresses in the geometric stiffness matrix, the hydrostatic stiffness matrix for a plate element is expressed as,

$$C_{ij} = C_{ij}^g + \int_{S_w} p_{,3} u_3^i u_3^j n_3 dS + \int_{S_{de}} \sigma_{33} u_3^i u_{3,k}^j n_k dS, \; k = 1, 2 \tag{2.58}$$

where $p_{,3} = -\rho g T_{33}$. T_{33} is the element of the transformation matrix $\mathbf{T}$, such that it transforms a vector from local coordinates to the global coordinates. S_{de} represents the four edges and dry surface. The geometric stiffness in Eq. (2.58) is defined as,

$$C_{ij}^g = \int_A N_{mn} u_{3,m}^i u_{3,n}^j dA,$$

$$N_{mn} = \int_{-t/2}^{t/2} \sigma_{mn} d\bar{z} - \delta_{mn} \int_{-t/2}^{t/2} \sigma_{33} d\bar{z}, \quad m, n = 1, 2. \tag{2.59}$$

Here, the integration is carried over the mid-plane area, A. δ_{mn} is the Kronecker delta function. The surface integral in Eq. (2.58) can be calculated along the mid-plane independently of $\bar{z}$, however, in Eq. (2.59) the distribution of the normal stress over the thickness is required.

2.5.3.2 Damping and added mass

For a structure near the free surface, the second term on the right-hand side of Eq. (2.52) represents the radiation forces, which can be given from Eqs. (2.22), (2.48) as,

$$\mathbf{f}_{Ri} = \text{Re}\left\{ \sum_{j=1}^{n_m} p_j e^{i\omega t} f_{ij} \right\}, \quad i = 1, 2, ..., n_m \tag{2.60}$$

where f_{ij} is the ith complex force component related with the jth mode shape and can be expressed as,

$$f_{ij} = \rho\omega^2 \iint\limits_{S_w} (\mathbf{n}.\mathbf{u}_i)\Phi_j dS = \omega^2 A_{ij} - i\omega B_{ij} \tag{2.61}$$

Here, A_{ij} and B_{ij} denote the generalized added mass and generalized hydrodynamic damping components, respectively:

$$A_{ij} = \rho \int\limits_{S_w} (\mathbf{n}.\mathbf{u}_i)\text{Re}\{\Phi_j\}dS \quad , \quad B_{ij} = -\rho\omega \int\limits_{S_w} (\mathbf{n}.\mathbf{u}_i)\text{Im}\{\Phi_j\}dS, \tag{2.62}$$

Considering the time harmonic dependency, the radiation force can be given from Eq. (2.61) as

$$\mathbf{f}_{Ri} = -\sum_{i=1}^{n_m} (A_{ij}\ddot{p}_i + B_{ij}\dot{p}_j) \tag{2.63}$$

The added-mass coefficients imply that the force component proportional to the acceleration, whereas, the damping coefficients signify the force proportional to the body velocity. Moreover, the added-mass and damping matrices are symmetric due to the implication of Green's theorem during the computation of the coefficients [28].

The added mass can be explained as a certain fluid volume that is accelerated by the response of the structure. Hypothetically, every fluid particle will be affected by the structural motions, and the added mass is a weighted integration of this entire mass. Unlike the body mass, the added mass differ with the direction of the body motion [28].

The damping related force results from the waves generated by the structural motions radiating outward on the free surface. Thus, the damping coefficients have a relation with the amplitude of the waves generated by the structure. If there is waves generated by the structure in any mode, the corresponding damping coefficient must be greater than zero [28].

2.5.3.3 Wave-exciting force

The wave exciting forces determined by the last term of Eq. (2.52) are proportional to the incident wave amplitude.

$$\Xi_H = -\rho \operatorname{Re}\left\{ i\omega\zeta e^{i\omega t} \iint_{S_w} (\Phi_I + \Phi_S)(\mathbf{n}.\mathbf{u}_i)\,dS \right\} \qquad (2.64)$$

It is appropriate to write Eq. (2.64) in the form,

$$\Xi_{Hi} = \operatorname{Re}\left\{ \zeta e^{i\omega t} X_i \right\}, \; i = 1, 2, .., n_m \qquad (2.65)$$

where X_i is the complex excitation forces in the ith principle mode for a unit amplitude of incident wave. Substituting the boundary condition (2.33) into Eq. (2.64) yields following expression,

$$X_i = -\rho \iint_{S_w} (\Phi_I + \Phi_S)\frac{\partial \Phi_i}{\partial n}\,dS \qquad (2.66)$$

The incident wave potential can be found for finite or infinite depth conditions by using Eq. (2.11). The similarity between boundary conditions for the scattering and incident wave potential can be used to derive the formulation for the excitation forces that is known as *Haskind relation* where no assumption required about wavelength or body geometry. Since the boundary condition at free surface and the radiation condition at infinity are the same for these two potentials, Green's theorem can be applied on the wetted surface for the scattering potential [28],

$$\iint_{S_w} \left(\Phi_i \frac{\partial \Phi_S}{\partial n} - \Phi_S \frac{\partial \Phi_i}{\partial n} \right) dS = 0, \quad i = 1, 2, ..., n_m. \qquad (2.67)$$

In this manner, one can rearrange the excitation force expression by substituting Eq. (2.67) into Eq. (2.66),

$$X_i = -\rho \iint_{S_w} \left(\Phi_I \frac{\partial \Phi_i}{\partial n} + \Phi_i \frac{\partial \Phi_S}{\partial n} \right) dS \qquad (2.68)$$

In order to reduce the unknown scattering velocity potential from the expression, the boundary condition (2.27) is imposed to Eq. (2.68) and the following Haskind relation is acquired.

$$X_i = -\rho \iint\limits_{S_w} \left(\Phi_I \frac{\partial \Phi_i}{\partial n} - \Phi_i \frac{\partial \Phi_I}{\partial n} \right) dS \qquad (2.69)$$

By this method, it is possible to state the excitation forces independently of the scattering potential, without approximation.

2.5.4 Floater response in frequency domain and RAO

Considering that the wave excitation is harmonic, the generalized equation of motion Eq. (2.24) can be given in the frequency domain that the response of the floater is represented through the response amplitude operator (RAO). By substituting Eq. (2.29) for the principle coordinates $\mathbf{p}$ and Eq. (2.65) for the excitation forces in Eq. (2.24), the equation of motion can be expressed as,

$$\left[-\omega^2 \left(\mathbf{a} + \mathbf{A}(\omega) \right) + i\omega \mathbf{B}(\omega) + \mathbf{c} + \mathbf{C} \right] \mathbf{p} = \zeta \mathbf{X}(\omega). \qquad (2.70)$$

where, ω is the incident wave frequency. The generalized fluid radiation and wave excitation forces are frequency dependent, so the RAO, as the principle coordinate vector, is computed for each incident wave frequency of interest using Eq. (2.70):

$$RAO(\omega) = \mathbf{p} \big/ \zeta = \left[-\omega^2 \left(\mathbf{a} + \mathbf{A}(\omega) \right) + i\omega \mathbf{B}(\omega) + \mathbf{c} + \mathbf{C} \right]^{-1} \mathbf{X}(\omega). \qquad (2.71)$$

The components of RAO represent the influence values of each normal mode of interest on the overall response for unit wave amplitude of a certain frequency.

2.6 Time Domain Hydrodynamics

The time domain floater hydrodynamics can be constituted by using the output of the frequency domain analysis. In other words, the frequency dependent radiation and excitation forces obtained through the linear hydroelastic analysis can be transformed into their time dependent form. Accordingly, the time domain equation of motion can be written in generalized coordinates as,

$$(\mathbf{a} + \mathbf{A}_\infty)\ddot{\mathbf{p}}(t) + (\mathbf{b} + \mathbf{B})\dot{\mathbf{p}}(t) + (\mathbf{c} + \mathbf{C})\mathbf{p}(t) = \mathbf{f}_W(t) + \mathbf{f}_R(t). \qquad (2.72)$$

Here, A_∞ is the generalized added mass matrix at infinite frequency, which has constant terms, and $\mathbf{f}_W(t)$ and $\mathbf{f}_R(t)$ are the time domain counterparts of the excitation and radiation forces, respectively.

The irregular sea state can be determined by the combination of regular wave components by using an appropriate wave spectrum. Within this context, the free surface elevation in an irregular sea can be given as [20]:

$$\zeta(t) = \frac{1}{2\pi} \int_{-\infty}^{\infty} W(\omega) \sqrt{2\pi S_\zeta^{2-Sided}(\omega)} e^{i\omega t} d\omega.$$ **(2.73)**

Here, $W(\omega)$ and $S_\zeta^{2-Sided}$ are the Fourier transform of a white Gaussian noise (WGN) time-series with standard normal distribution and two-sided power spectral density (see further details in Ref. [20]). The excitation forces, then can be estimated as,

$$\mathbf{f}_{Wi}(t) = \frac{1}{2\pi} \int_{-\infty}^{\infty} W(\omega) \sqrt{2\pi S_\zeta^{2-Sided}(\omega)} X_i(\omega, \beta) e^{i\omega t} d\omega$$ **(2.74)**

where $X_i(\omega, \beta)$ is the complex wave-excitation forces on the floater due to unit amplitude incident wave with frequency ω and direction β.

The time domain representation of the radiation forces is given by the convolution integral,

$$\mathbf{f}_{Ri}(t) = -\int_0^t K_{ij}(\tau) \dot{p}_j(t-\tau) d\tau.$$ **(2.75)**

Here, τ is a dummy variable and K_{ij} is the radiation IRF, covering the effects of the hydrodynamic damping as well as remaining part of added mass when A_∞ is subtracted. It can be found by the Fourier sine transformation:

$$K_{ij}(t) = -\frac{2}{\pi} \int_0^{\infty} \omega \left[A_{ij}(\omega) - A_\infty \right] \sin(\omega t) d\omega$$ **(2.76)**

The convolution integral represents that the memory effects that describe the influence of radiation forces through the motion history of the floater.

2.7 Aerodynamics of the Rotor

The dynamics of fluid passing through the wind turbine is represented by the Navier-Stokes equations. These equations, however, are not applied for the design and aerodynamic analysis of FOWTs due to the computational complexity they introduce. Instead, wind turbine aerodynamics is generally investigated through the two-dimensional airfoil analysis with quasi-steady flow by using the BEMt [25].

The BEMt combines the momentum theory that expresses the momentum balance on a rotating circular stream tube passing through the rotor and the blade element theory that computes the forces on the rotor by integrating the individual forces on the airfoil at each defined section of the blade [36].

2.7.1 Momentum theory

In the momentum theory, the rotor is considered as a collection of infinite number of very thin blades without drag, i.e. an actuator disk, where the static pressure has discontinuity at its sides due to energy extraction. The system illustrated in Figure 2.4 is represented in a fixed control volume whose boundaries defined by the stream tube. The theory assumes that the wind is steady, homogenous and unidirectional; the flow in control volume is potential and uniform across the actuator disk; upwind and downwind (station 1 and 4 respectively in Figure 2.4) boundaries are far enough from the actuator disk so that the air pressure is equal to the atmospheric pressure at these boundaries [25].
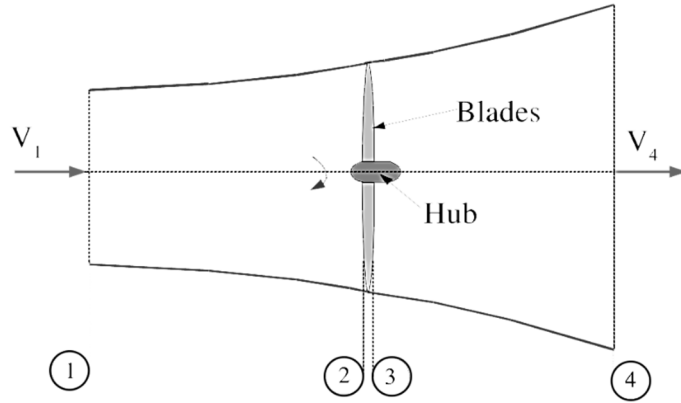
Figure 2.4 : Stream tube around the rotor [36].

Assuming the pressures at station 1 and 4 and the velocities at station 2 and 3 are equal and flow is frictionless, the Bernoulli's equation yields [36]

$$p_2 - p_3 = \frac{1}{2}\rho\left(V_1^2 - V_4^2\right) \tag{2.77}$$

where, p, V and ρ stand for the pressure, flow velocity and density of the air, respectively, while the attached indices refer to the related stations. The axial force can be expressed, then, as follows

$$dF_x = \frac{1}{2}\rho\left(V_1^2 - V_4^2\right)dA \tag{2.78}$$

29

An axial induction factor, α, is defined by the fractional decrease of the velocity when the wind reaches to the actuator disk,

$$\alpha = \frac{V_1 - V_2}{V_1} \tag{2.79}$$

or equivalently,

$$V_2 = V_1(1-\alpha) \tag{2.80}$$

$$V_4 = V_1(1-2\alpha) \tag{2.81}$$

By substituting Eq. (2.81) into Eq. (2.78) and rewriting the far field wind velocity as $V_1 = V$, the axial thrust can be written as follows.

$$dF_x = \frac{1}{2}\rho V^2 \left[4\alpha(1-\alpha)\right]2\pi r dr \tag{2.82}$$

The extracted power by the rotor, then, is expressed as,

$$P = \frac{1}{2}\rho A V^3 4\alpha(1-\alpha)^2 \tag{2.83}$$

The non-dimensional power coefficient is given as,

$$C_P = \frac{P}{\frac{1}{2}\rho A V^3} \tag{2.84}$$

Substituting Eq. (2.84) into Eq. (2.83) yields,

$$C_P = 4\alpha(1-\alpha)^2. \tag{2.85}$$

The maximum power coefficient of the ideal rotor, known as Betz limit, can be found as $C_{P\max} = 0.5926$ according to Eq. (2.85). In practice, the wake rotation, finite numbers of blades and aerodynamic drag prevent to achieve this efficiency.

The wake rotation effects due to the blade rotation, neglected so far herein, are taken into account by using the conservation of the angular momentum. Considering the angular velocities of the wake rotation ω, blade rotation Ω, the moment of inertia $I = mr^2$, the angular momentum $L = I\omega$, and the torque $T = dL/dt$, the following relation can be written:

$$T = \frac{d(I\omega)}{dt} = \frac{d(mr^2\omega)}{dt} = \frac{dm}{dt}r^2\omega \tag{2.86}$$

Here, m and r are the mass of the air and radius of the circular element illustrated in Figure 2.5b in stream tube, respectively. For the rotating circular differential element, the torque expressed as,

$$dT = d\dot{m}\omega r^2 = \rho V_2 \omega r^2 2\pi r dr \tag{2.87}$$

By defining the angular induction factor as $\alpha' = \omega/2\Omega$ and substituting Eq. (2.80) into Eq. (2.87), the torque equation can be rearranged as,

$$dT = 4\alpha'(1-\alpha')\rho V \Omega r^3 \pi dr \tag{2.88}$$

The 1/2 factor used in the angular induction factor is due to averaging the angular velocities of the wake at two sides of the rotor [25]. The axial and tangential forces, given by Eqs. (2.82) and (2.88), respectively, on a circular element can be derived by using the momentum theory.

2.7.2 Blade element theory

The blade element theory relies on the computation of the forces on the rotor by dividing the blades into sufficient number of element along the blade length and analyzing each element independently. The aerodynamic interaction between the blade elements is neglected and the forces are determined by using the lift and drag coefficients at cross-section of each blade element. In order to obtain the lift and drag
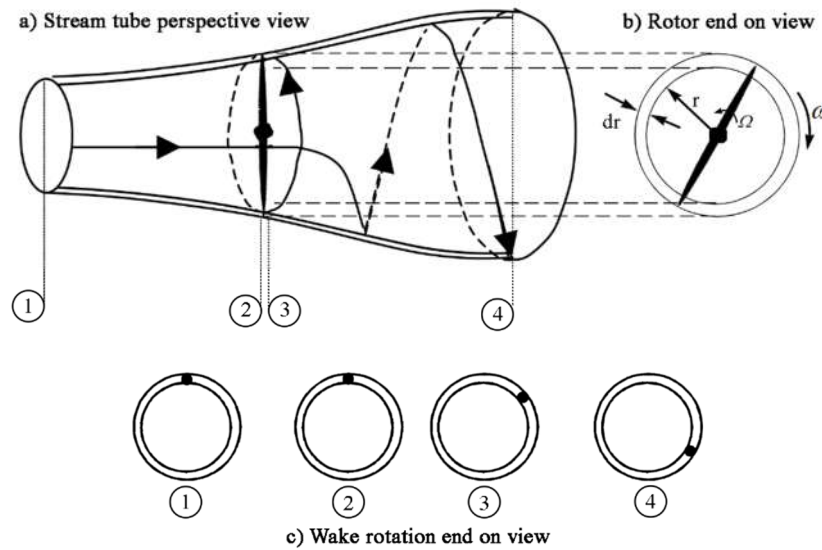

Figure 2.5 : Rotating circular stream tube and notation [25, 36].

coefficients of the cross-section, the airfoils data can be used, if available, otherwise wind tunnel experiment is required.

A typical blade discretization is illustrated in Figure 2.6. Each blade element is subjected to different airflow depending on the chord length, c, twist angle, γ, and position and velocity of the element [36]. Thus, the relative flow should be determined before the aerodynamic calculation of the corresponding airfoil.

The flow reaching the blade element at station 2 of the stream tube is initialy non-rotating and it leaves the rotor with rotational velocity ω. The rotational flow over the airfoil can be determined by averaging the inlet and outlet velocities. Considering that the blade rotates with velocity Ω and recalling the angular induction factor $\alpha' = \omega/2\Omega$, the average tangential velocity can be expressed as

$$V_\theta = \Omega r + \frac{1}{2}\omega r = \Omega r(1+\alpha') \qquad (2.89)$$

The incoming flow orientation can be determined by using the normal and tangential velocities. By substituting normal velocity in Eq. (2.80), the flow orientation can be written as follows,

$$\tan\beta = \frac{\Omega r(1+\alpha')}{V(1-\alpha)} \qquad (2.90)$$

where, β, as seen in Figure 2.7, represents the angle between the directions of the wind and the flow over the blade element. By defining the local tip speed ratio as $\lambda_r = \Omega r/V$, Eq. (2.90) is rewritten in the following form:
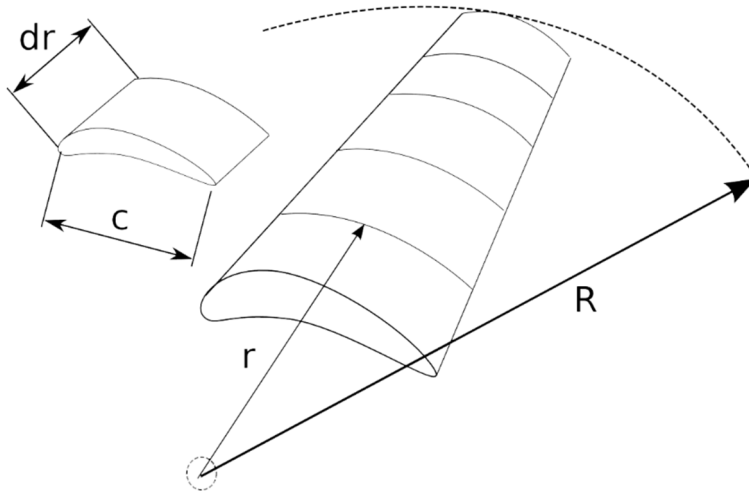

Figure 2.6 : Blade Element Model [36].

$$\tan \beta = \frac{\lambda_r (1+\alpha')}{(1-\alpha)} \tag{2.91}$$

The incoming flow *W*, thus, is given as,

$$W = \frac{V(1-\alpha)}{\cos \beta} \tag{2.92}$$

The drag force is parallel to the incoming waves, whereas the lift and drag forces are perpendicular to each other. The forces on the blade element, illustrated in Figure 2.7, can be expressed in terms of lift and drag forces as,

$$dF_x = dL \sin \beta + dD \cos \beta \tag{2.93}$$

$$dF_\theta = dL \cos \beta - dD \sin \beta \tag{2.94}$$

where, *dL* and *dD* are the lift and drag forces on each element:

$$dL = C_L \frac{1}{2} \rho W^2 c dr \tag{2.95}$$

$$dD = C_D \frac{1}{2} \rho W^2 c dr \tag{2.96}$$

Here, C_L and C_D are the lift and drag coefficients of the corresponding airfoil, respectively.

Finally, Eqs. (2.91)-(2.96) yield the following torque and thrust force expressions:
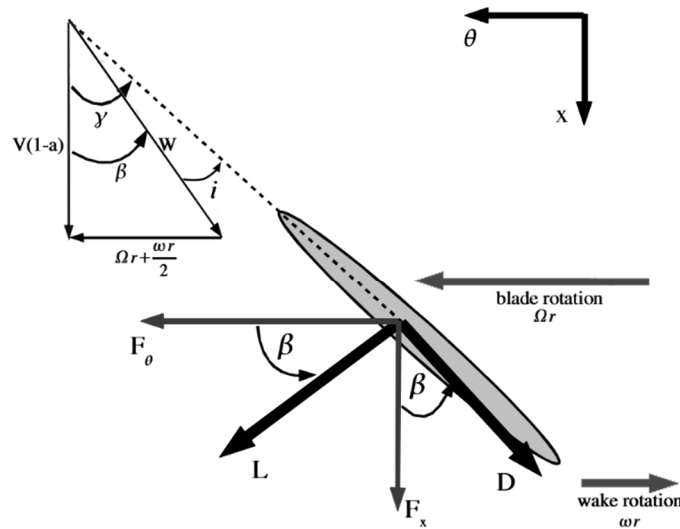

Figure 2.7 : Flow and forces on the airfoil [36].

33

$$dF_x = \sigma' \pi \rho \frac{V^2 (1-a)^2}{\cos^2 \beta} (C_L \sin \beta + C_D \cos \beta) \, r \, dr \qquad \textbf{(2.97)}$$

$$dT = \sigma' \pi \rho \frac{V^2 (1-a)^2}{\cos^2 \beta} (C_L \cos \beta - C_D \sin \beta) r^2 \, dr \qquad \textbf{(2.98)}$$

Here, $\sigma' = Bc/2\pi r$ is known as the local solidity, with B as the number of blades.

2.7.3 Blade element momentum theory

The rotor aerodynamics whose blade geometric properties (i.e. airfoil geometry, blade length and twist distribution along the blade length) are known can be analyzed by combining the momentum and blade element theories. Before equating the thrust and torque expressions, equation of the momentum theory should be adjusted to represent the finite number of blades. This adjustment is commonly applied by tip loss factor. The tip loss factor is expressed as follows [25, 36]:

$$Q = \frac{2}{\pi} \cos^{-1} \left[\exp \left\{ -\left(\frac{B/2[1-r/R]}{(r/R)\cos \beta} \right) \right\} \right] \qquad \textbf{(2.99)}$$

By substituting the tip loss factor in Eqs. (2.82)-(2.88), the thrust and torque equations become,

$$dF_x = Q\rho V^2 \left[4\alpha (1-\alpha) \right] \pi r dr \qquad \textbf{(2.100)}$$

$$dT = Q 4\alpha'(1-\alpha') \rho V \Omega r^3 \pi dr. \qquad \textbf{(2.101)}$$

By equating the adjusted expressions of the momentum theory in Eqs. (2.100)-(2.101) and the blade element expressions in Eqs. (2.97)-(2.98), the following BEMt equations are derived.

$$\frac{a}{1-a} = \frac{\sigma'[C_L \sin \beta + C_D \cos \beta]}{4\cos^2 \beta} \qquad \textbf{(2.102)}$$

$$\frac{a'}{1-a} = \frac{\sigma'[C_L \cos \beta - C_D \sin \beta]}{4\lambda_r \cos^2 \beta} \qquad \textbf{(2.103)}$$

The aerodynamic performance of the rotor can be determined by using Eqs. (2.102)-(2.103). The power output of the rotor is expressed as,

$$P = \int_{r_h}^{R} dP dr = \int_{r_h}^{R} \Omega dT dr \qquad \textbf{(2.104)}$$

34

where, r_h is the hub radius. The dimensionless power coefficient C_P is given by,

$$C_P = \frac{P}{P_{wind}} = \frac{\int_{r_h}^{R} \Omega dT dr}{\frac{1}{2}\rho \pi R^2 V^3} \tag{2.105}$$

Substituting the torque statement to Eq. (2.105) yields the power coefficient equation in terms of tip speed ratios.

$$C_P = \frac{8}{\lambda^2} \int_{\lambda_h}^{\lambda} Q \lambda_r^3 \alpha'(1-\alpha)\left[1 - \frac{C_D}{C_L}\tan\beta\right]d\lambda_r. \tag{2.106}$$

Here, λ and λ_h indicate the blade and hub tip speed ratios that express the ratio of the related element speed to the far field wind speed.

2.8 Dynamic Response of the Floater

The response of the floater to the combined wave and wind loads can be obtained through the equation of motion given in Eq. (2.72) by adding the forces transferred from RNA. The equation of motion takes the following form,

$$(\mathbf{a} + \mathbf{A}_\infty)\ddot{\mathbf{p}}(t) + (\mathbf{b} + \mathbf{B})\dot{\mathbf{p}}(t) + (\mathbf{c} + \mathbf{C})\mathbf{p}(t) = \mathbf{f}_W(t) + \mathbf{f}_R(t) + \mathbf{f}_A(t). \tag{2.107}$$

Here, $\mathbf{f}_A$ is the generalized aerodynamic force that represents the forces transferred from RNA and given as,

$$\mathbf{f}_A(t) = \mathbf{U}^T f_i \tag{2.108}$$

where f_i is the nodal forcing vector. The aerodynamic forcing term includes the interaction forces of the blades with the air flow so that the motion of the RNA should be considered during the BEMt solution. Therefore, a weakly coupling procedure between hydrodynamic and aerodynamic analysis is formed by setting an interface point on tower top, where forces on the RNA are transmitted to the structure and in return, the motion of RNA is updated according to the structural response.

The coefficients of the structural damping $\mathbf{b}$ can be estimated by the relation,

$$b_{ij} = 2\zeta c_{ij}\sqrt{\frac{a^*_{jj}}{c_{jj}}} \tag{2.109}$$

where ζ stands for the structural damping ratio. a^*_{jj} and c_{ij} are the coefficient of the mass matrix excluding the RNA mass and stiffness matrix, respectively. The term in square root represents the natural frequencies of the structure when RNA mass is not included.

For the time integration, the equation of motion can be converted into a set of first-order differential equations by defining the state variable

$$\mathbf{x}(t) = \begin{Bmatrix} \mathbf{p}(t) \\ \dot{\mathbf{p}}(t) \end{Bmatrix}. \tag{2.110}$$

The state-space formulation of the equation of motion can be given as [37],

$$\dot{\mathbf{x}}(t) = \mathbf{A}\mathbf{x}(t) + f(t) \tag{2.111}$$

where,

$$\mathbf{A} = \begin{bmatrix} 0 & I \\ -(\mathbf{a} + \mathbf{A}_\infty)^{-1}(\mathbf{c} + \mathbf{C}) & -(\mathbf{a} + \mathbf{A}_\infty)^{-1}(\mathbf{b} + \mathbf{B}) \end{bmatrix},$$

$$f(t) = \begin{Bmatrix} 0 \\ -(\mathbf{a} + \mathbf{A}_\infty)^{-1}(\mathbf{f}_W(t) + \mathbf{f}_R(t) + \mathbf{f}_A(t)) \end{Bmatrix}. \tag{2.112}$$

The influence of the hydrodynamic added-mass on the structural response is significant due to the same order of densities of the water and structural material; in contrast, by considering the air density, the aerodynamic added-mass can be excluded from the equation [20]. However, both aerodynamic and hydrodynamic damping are considered. Eq.(2.111) can be integrated using the explicit 4th order Runge-Kutta method and at each time step, the structural response can be obtained.

3. NUMERICAL APPLICATION

The time domain response analysis of the large-scale support structure carrying two of 5MW wind turbines is performed under combined wave and wind loads by coupling the hydroelastic and aeroelastic solution procedures.

Firstly, the dynamic characteristics of the structure, i.e. natural frequencies and mode shapes, are obtained by the finite element method (FEM) in order to represent the structural response and corresponding fluid perturbation by the modal expansion method. The hydrodynamic forces on wave-structure interface are stated by the boundary integral equation (BIE) considering the linear waves and solved by Boundary Element Method (BEM) for the given frequency interval. The resulting frequency dependent interaction and excitation forces are converted into their time domain counterparts. The fluid-structure-interaction forces are calculated by the convolution integral of the impulse response functions that are obtained from the radiation forces in frequency domain by using the Filon quadrature. The time domain representation of the excitation forces for the irregular incident waves is obtained by the Fourier transformation of the wave exciting forces corresponding to the unit wave amplitude. Here, the Pierson-Moskowitz wave spectrum is applied for the specified wind velocity. The aerodynamic forces on the rotor are obtained by the Blade Element Momentum Theory (BEMt). The time integration of the structural responses are computed by forming the state-space model.

3.1 Verification

In this section, the computation procedure for the solution of the radiation and diffraction problems is tested by considering a free-floating cylinder near the free surface, which is commonly used for verification. Furthermore, the RAOs of a box-like VLFS are calculated and compared with the benchmark data in order to verify the wave force and RAO computation procedure [38].

The cylinder with radius $r = 1$ m and draught $T = 1$ m is discretized by using three different meshes of 272, 612 and 2041 elements (Figure 3.1), in order to analyze the
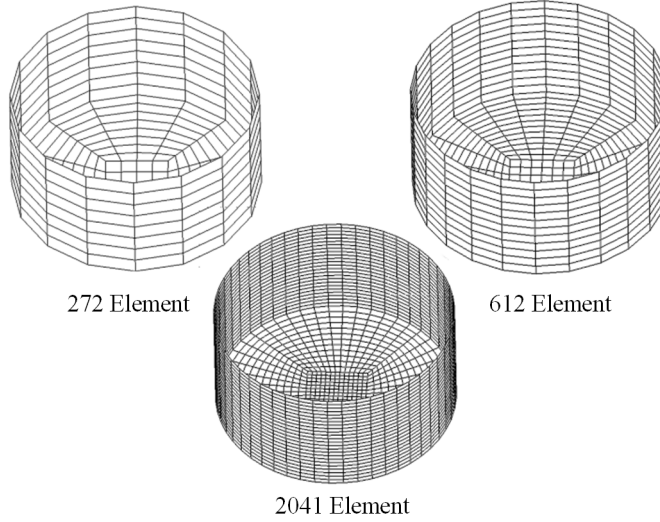
Figure 3.1 : Cylinder meshes used in BEM solution procedure

convergence of the results. Firstly, the non-dimensional added mass and hydrodynamic damping coefficients of the vertical cylinder body are computed by considering only the rigid body modes for the frequency interval [0, 10] rad/s. Then, the exciting forces, i.e. the diffraction forces, and the RAOs of the surge, heave and pitch motions are obtained. The damping due to viscous effects is imitated by adding an external damping coefficient for the pitch motion. The main parameters of the cylinder are given in Table 3.4.

The obtained results are compared with the results presented in [39]. The non-dimensional added mass and damping coefficients are determined as follows.

$$\bar{a}_{ij} = \frac{a_{ij}}{\rho \pi r^2 T}, \ \bar{b}_{ij} = \frac{b_{ij}}{\rho \pi r^2 T \omega} \ \text{ for } i, j \le 3$$

$$\bar{a}_{ij} = \frac{a_{ij}}{\rho \pi r^3 T}, \ \bar{b}_{ij} = \frac{b_{ij}}{\rho \pi r^3 T \omega} \ \text{ for } i, j \ge 4$$

(3.1)

Table 3.1 : Characteristics of the cylinder [39].

Radius	1.00 m	COG X coordinate	0.00 m
Draught	1.00 m	COG Y coordinate	0.00 m
Mass	3.14E+3 kg	COG Z coordinate	-0.50 m
Pitch inertia	1.57E+3 kg m^2	C$_{55}$ (External damping coefficient)	4.35E+3 kg m^2/s

The added mass and damping coefficients of the surge, heave and pitch motion are presented in Figure 3.2, along with the results found in literature. The results indicate

the improvement of the accuracy in parallel with the mesh density. The added mass
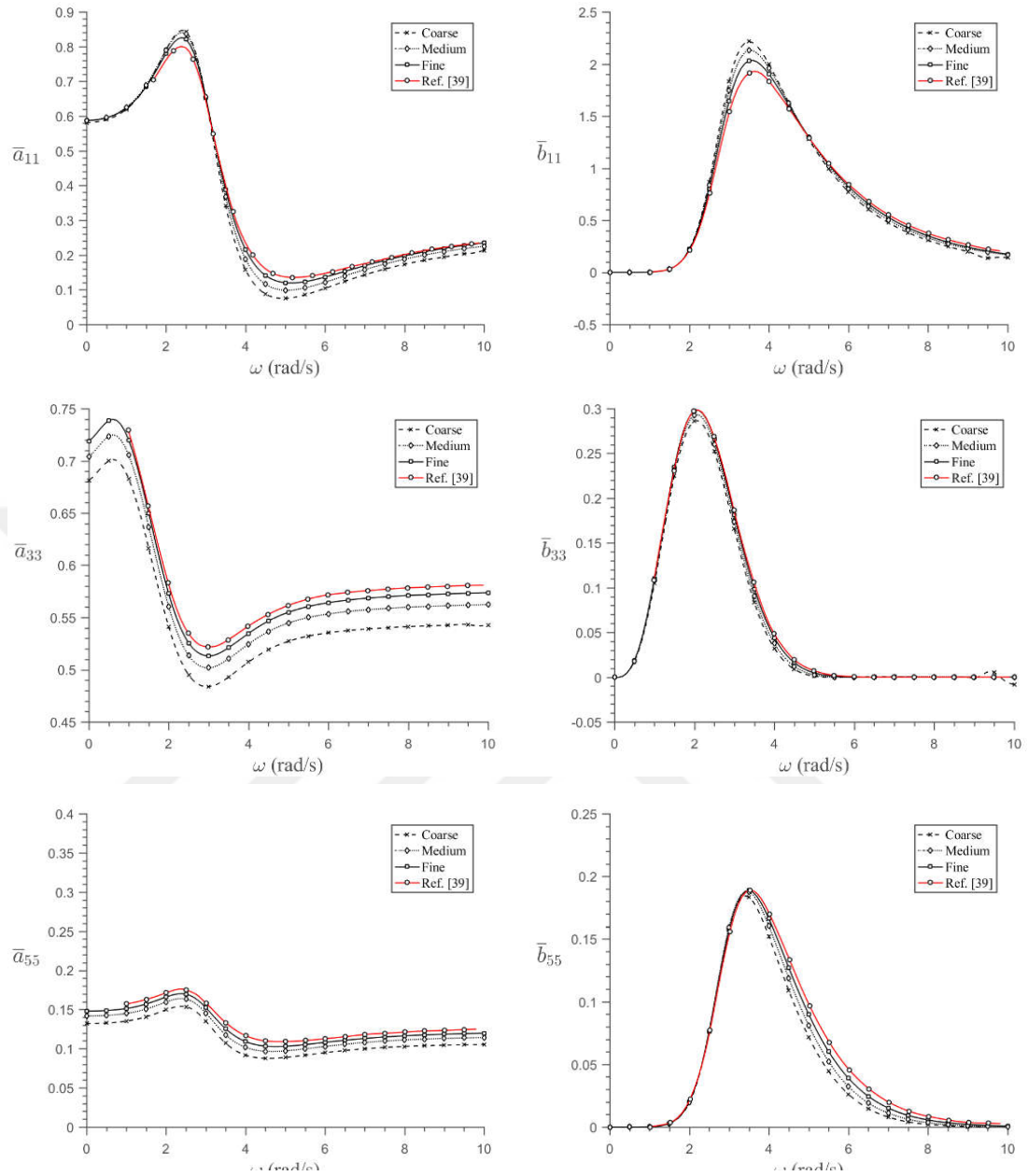
Figure 3.2 : Convergence of the radiation coefficients for the cylinder.

coefficients of the fine mesh in the pitch motions, $\overline{a}_{55}$, are slightly different due to the different mesh. This disagreement can be suppressed by intensifying the meshes near the free surface or using quadratic boundary elements.

The wave exciting forces and RAOs for heave and pitch motions of the cylinder are calculated for the incident wave frequencies of [0-10] rad/s interval. The obtained results and the comparisons are presented in Figure 3.3 and Figure 3.4. The non-dimensional forces and moments are determined as follows
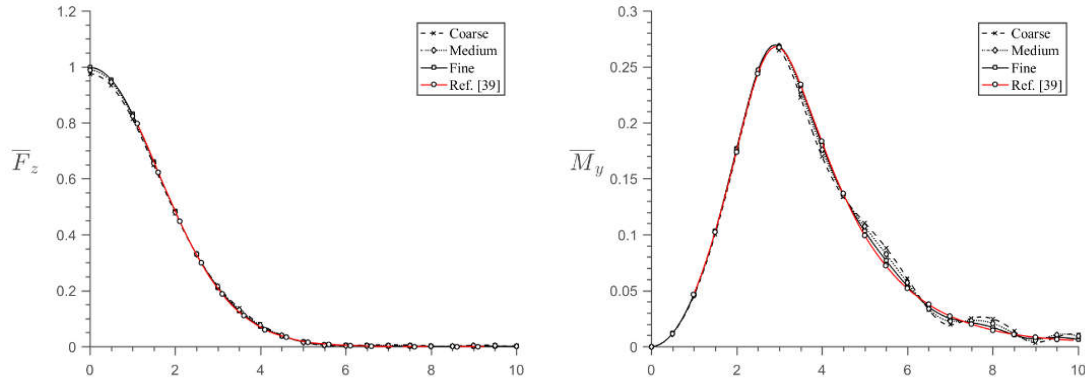
Figure 3.3 : Convergence of the wave exciting forces for the cylinder.

$$\overline{F}_z = \frac{f_z}{\rho g \pi r^2 T} \;,\; \overline{M}_y = \frac{m_y}{\rho g \pi r^3 T} \tag{3.2}$$

Although the minor differences are observed in wave exciting forces for the coarse and medium meshes, the results are quite compatible for the finest mesh. On the other side, the RAOs of the pitch motion have some differences probably due to the slight differences in added-mass and damping coefficients, yet the RAOs give consistent results in general.

So far, the solution procedure of the rigid body motions is verified; however, the varication should be extended to include the elastic motions of the structure. In this respect, the hydroelastic analysis of a VLFS is performed to obtain RAOs. The structural and hydrodynamic descriptions of the selected VLFS are presented in Table 3.5. The resulting RAOs are compared with the benchmark case given in Ref. [38]. The bending stiffness of the elements used in dry analysis is increased by considering that the bending thickness is five times of the nominal plate thickness. The density of
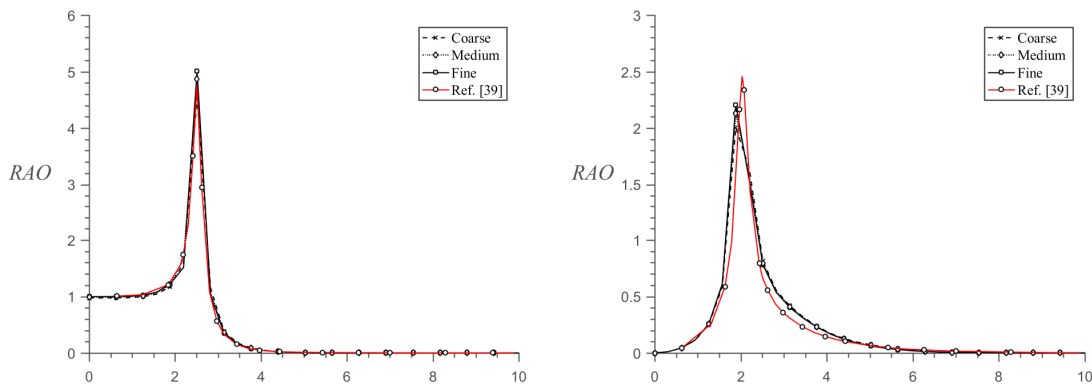

Figure 3.4 : Convergence of the RAOs for the VLFS.

the bottom and top decks are set to 15375 kg/m^3 and 5125 kg/m^3, while the other plates are considered massless. The element size are 1 m in horizontal directions and 0.5 m in vertical direction. The coordinate system is located at still water level at midship with *x*-axis is along the longitudinal direction and *z*-axis is pointing upward. The analysis is conducted by considering the first twelve elastic modes. The resulting RAOs in first vertical mode of the VLFS is presented in Figure 3.5 for two different incident wave angle.

Table 3.2 : Structural and hydrodynamic characteristics of the VLFS.

Length	100 m	Elastic Modulus	15 GPa
Breadth	10 m	Poisson's Ratio	0.3
Height	2 m	Center of Gravity	(0.0, 0.0, 0.5) m
Draught	1 m	Density of water	1025 kg/ m3
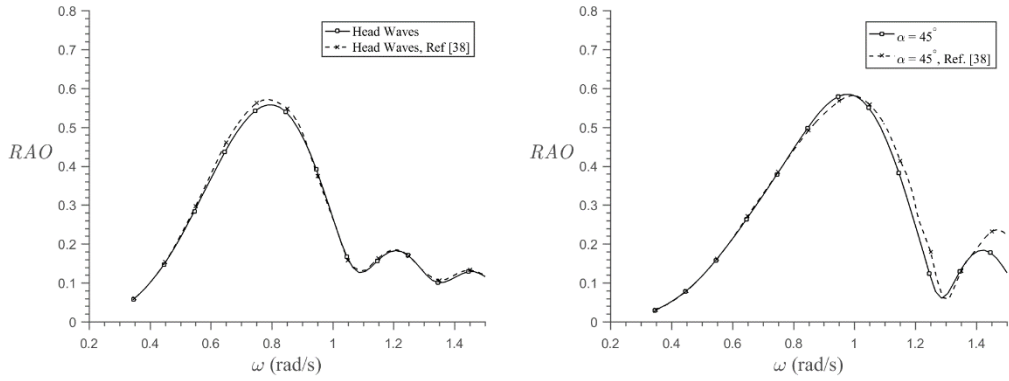
Figure 3.5 : RAO of the first vertical bending mode.

3.2 Modelling Approach

3.2.1 Dynamic characteristics and simplified structural model

For the computation of the dynamic characteristics of the FOWT, the finite element models of the floater and tower are based on shell and beam elements, respectively, and the RNAs are represented as concentrated masses with rotational inertia at tower-top. Since the yaw angle of the RNA influences the dynamic characteristics, the mode shapes of the structure are determined for each environmental condition according to the orientation of the RNA.

Typical arrangement of the floating structure contains longitudinal and transverse structural components as well as bottom and deck plating. The entire structural model

could be formed, yet for large structures this implies a large amount of redundant degrees of freedom; using simplified models is quite common [8] to avoid excessive computational cost for the hydroelastic response analysis, which is the adopted strategy here.

The structure can be idealized as equivalent orthotropic plate model by using uniform shell elements with identical bending and torsional stiffness. The following moment curvature equation can be written for two-dimensional structural elements,

$$
\begin{Bmatrix} M_x \\ M_y \\ M_{xy} \end{Bmatrix} = \begin{bmatrix} D_x & D_{xy} & 0 \\ D_{yx} & D_y & 0 \\ 0 & 0 & G_{xy} \end{bmatrix} \begin{Bmatrix} -\dfrac{\partial^2 w}{\partial x^2} \\ -\dfrac{\partial^2 w}{\partial y^2} \\ -2\dfrac{\partial^2 w}{\partial x \partial y} \end{Bmatrix}
\tag{3.3}
$$

where w is the global deflection of the structure, M_x and M_y are the biaxial bending moment, M_{xy} is the torsional moment, and the coefficients in matrix are the structural properties known as bending stiffness. For an orthotropic material, the stress-strain relation under plane-stress conditions are given as,

$$
\begin{Bmatrix} \sigma_x \\ \sigma_y \\ \tau_{xy} \end{Bmatrix} = \begin{bmatrix} \dfrac{E_1}{1-v_{12}v_{21}} & \dfrac{v_{21}E_1}{1-v_{12}v_{21}} & 0 \\ \dfrac{v_{12}E_1}{1-v_{12}v_{21}} & \dfrac{E_2}{1-v_{12}v_{21}} & 0 \\ 0 & 0 & G_{12} \end{bmatrix} \begin{Bmatrix} \varepsilon_x \\ \varepsilon_y \\ \gamma_{xy} \end{Bmatrix}
\tag{3.4}
$$

where E_1 and E_2 are the elastic modulus in longitudinal and transverse directions, respectively, and v_{12} and v_{21} are the Poisson ratios. The moment-curvature relation of the equivalent orthotropic plate model is expressed as follows,

$$
\begin{Bmatrix} M_x \\ M_y \\ M_{xy} \end{Bmatrix} = \frac{t^3}{12} \begin{bmatrix} \dfrac{E_1}{1-v_{12}v_{21}} & \dfrac{v_{21}E_1}{1-v_{12}v_{21}} & 0 \\ \dfrac{v_{12}E_1}{1-v_{12}v_{21}} & \dfrac{E_2}{1-v_{12}v_{21}} & 0 \\ 0 & 0 & G_{12} \end{bmatrix} \begin{Bmatrix} -\dfrac{\partial^2 w}{\partial x^2} \\ -\dfrac{\partial^2 w}{\partial y^2} \\ -2\dfrac{\partial^2 w}{\partial x \partial y} \end{Bmatrix}
\tag{3.5}
$$

where t is the equivalent orthotropic plate thickness. By considering the relation $v_{12}E_2 = v_{21}E_1$ and with an arbitrary value of t, Eq. (3.3) and Eq. (3.5) together provides the equivalent orthotropic plate properties, namely E_1, E_2, v_{12}, G_{12}.

Material properties of the shell elements are determined by using the orthotropic plate model in order to avoid a detailed structural model. However, the bulkheads of the structure is considered in 3-D model. The mass element properties are determined according to the NREL 5MW baseline turbine and the density of the tower is increased to represent the mass except its outer shell. The structural properties of the FE model are presented in Table 3.1.

Table 3.3 : Structural Properties.

Length x breadth x height	240 m x 24 m x 4 m
Draught	2 m
Bending stiffness of shell and bulkhead plates	5,0802E+09
Displacement	1,5744E+04 tonnes
Tower height	87,6 m
Tower mass	347.460 kg
Tower base radius / thickness	3 m / 27 mm
Tower top radius / thickness	1,935 m / 19 mm
Elastic modulus of tower material	210 GPa
Poisson ratio of tower material	0,3
Density of tower material	8500
RNA mass	3,5000E+05 kg
RNA roll inertia	4,5050E+07 kg m^2
RNA pitch inertia	2,4940E+07 kg m^2
RNA yaw inertia	2,5477E+07 kg m^2

The mode shapes of the structure can be described as either tower or platform type depending on the domination of the components. The platform type modes are identified as vertical (V), horizontal, (H), or torsional (T), and the tower type modes are identified as fore-aft (FA), side-to-side (SS), or mixed (MX), which states that the mode shape is directed along the *x*-axis, y-axis, or both, respectively. Some platform type modes are illustrated according to the RNA orientation (α) in Figure 3.6.
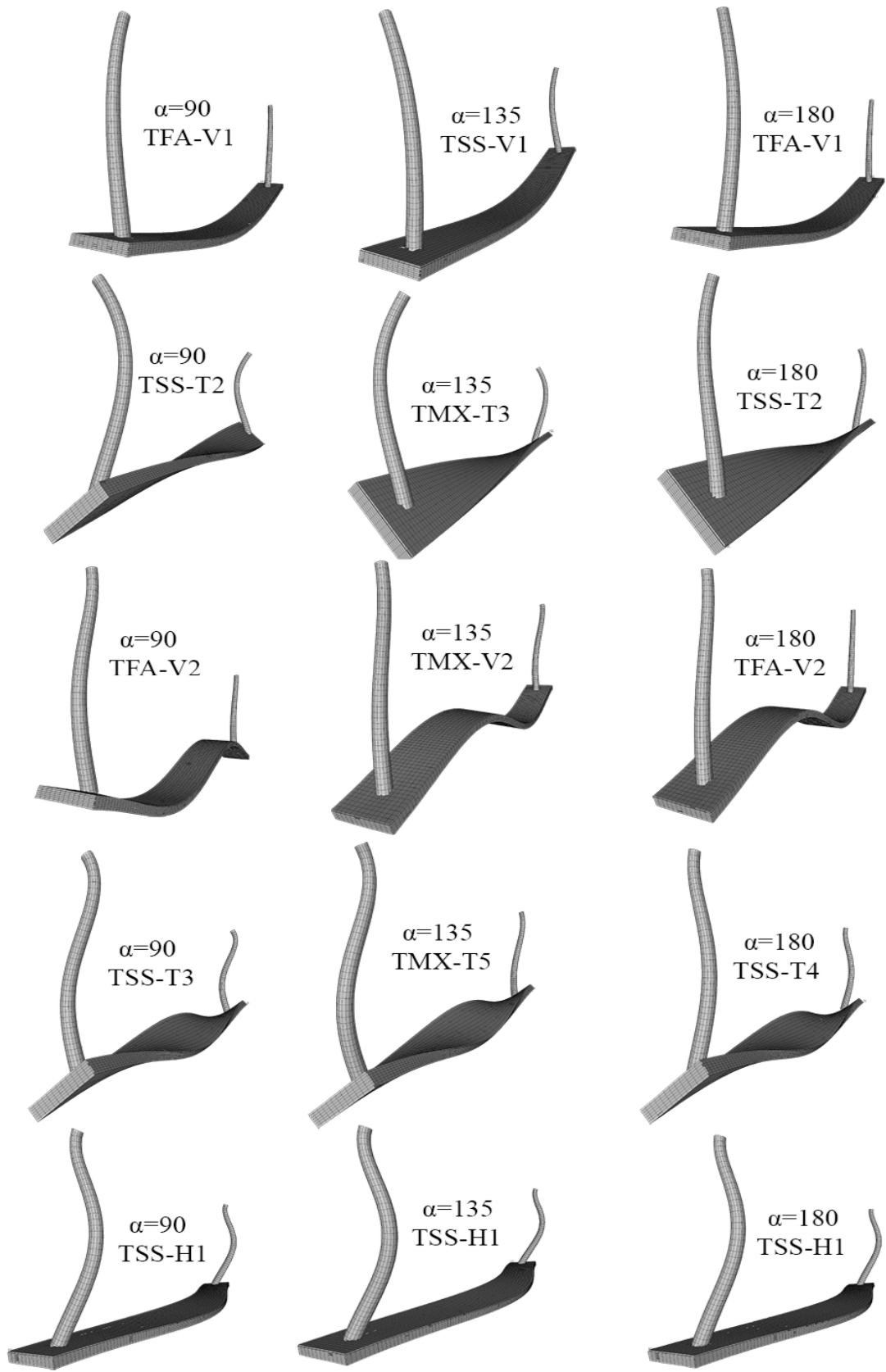
Figure 3.6 : Platform type mode shapes for different RNA orientation.

3.2.2 Boundary element model

The BE meshes are constructed according to the FE meshes so that the finite and boundary elements over the wetted surface match to each other. The tower type mode shapes are not considered in BE solutions, since their effect on the hydrodynamic analysis can be neglected.

BEM computation introduces inherently the irregular frequencies due to the implementation of the free surface Green function. Since the Green function satisfies the free surface boundary condition over the entire free surface-both the external free surface and assumed inner free surface, the obtained fluid forces are erroneous at the wave frequencies coinciding with the associated sloshing frequencies. In order to handle this problem during the BEM computation, the inner free surface is appended to the computation domain and a rigid wall boundary condition is applied over it. The potential distributions over the wetted boundary elements and inner water-plane boundary elements are represented by using linear and quadratic shape functions, respectively.

Considering that the free-terms in Eq. (2.47) are determined by only the geometry of the boundary surface, they can be calculated indirectly by considering a completely closed fluid domain–by combining the wetted surface and inner free surface–and applying constant potential in the domain so that the flux values in Eq. (2.48) vanishes for the corresponding internal flow problem. In that case, sum of the each rows of the **H** matrix must be zero and the diagonal terms of **H** can be calculated as [33],

$$H_{ll} = 1 - \sum_{n=1;n\neq l}^{E} H_{ln}.$$ **(3.6)**

Here, instead of the free surface Green function, the simple source of $1/4\pi r$ is used as the fundamental solution.

3.2.3 FAST and blade element model

The source code FAST is utilized in the implementation of the aerodynamics and structural dynamics of RNA. The nonlinear aeroelastic analysis is modeled in FAST according to the Kane's equation of motion for a simple holonomic system stated by the following equation [40, 41],

$$\mathbf{M}(p,u,t)\ddot{p} + \mathbf{f}(p,\dot{p},u,u_d,t) = 0$$ **(3.7)**

where $\mathbf{M}$ is the mass matrix, $\mathbf{f}$ is the forcing vector, u and u_d are the wind turbine control inputs and wind inputs [41]. FAST is set to consider the two flapwise and one edgewise elastic modes per blade, generator azimuth, shaft torsion, and nacelle yaw rotation. In order to compute the RNA forces due to each turbine, the tower top motions from hydroelastic analysis and kinematics obtained from the dynamic characteristics are imposed to the FAST dynamic routine. The forces on tower top due to RNA, except its gravity forces already accounted in FE model, are transferred to the hydroelastic analysis of the structure. BEMt computation is carried out by ignoring the aerodynamic interaction between the rotors.

Three bladed NREL 5MW wind turbine is adopted for the RNA model whose specifications are given in Table 3.2.

<div align="center">

Table 3.4 : RNA properties.

|	
Blades length	61,5 m
Mass of each blade	17.740 kg
Hub mass	56.780 kg
Nacelle mass	240.000 kg
Rated rotor speed	13,6 rpm
Blade passing frequency	0,68 Hz

</div>

3.2.4 Environment

In order to estimate the sea state, the Pierson-Moskowitz wave spectrum is implemented by considering 12 m/s wind speed. The wave parameters of the spectrum data are given in Table 3.3. The same direction is assumed for the wind and wave environments. Three incident angles are considered for the analysis, namely, 90° (beam), 135° (oblique) and 180° (head).

<div align="center">

Table 3.5 : Pierson-Moskowitz wave spectrum data.

|	
Wind speed	12 m/s
Significant wave height	3,074 m
Peak spectral period	7,338 s

</div>

3.3 Dynamic Response Analysis of FOWT

In order to observe the aero-hydro-elastic behavior of the floater carrying two 5MW wind turbines under wave and wind loads, firstly, the dynamic characteristics and the
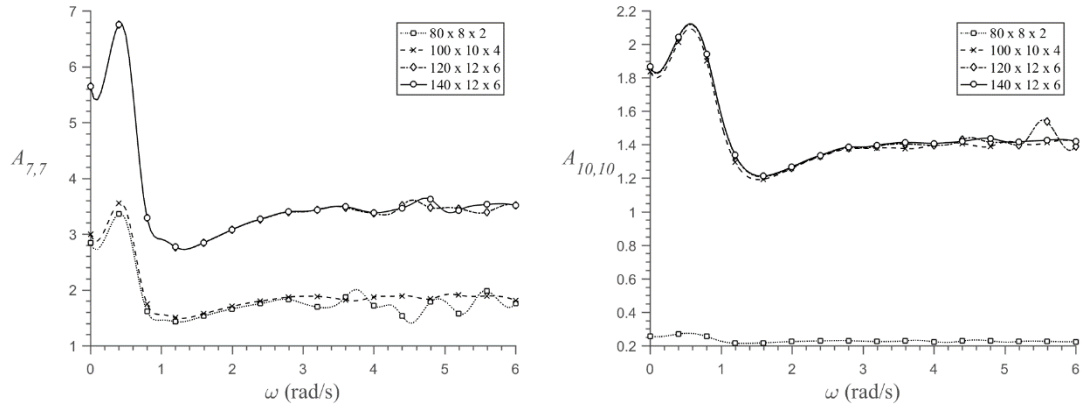
Figure 3.7 : Convergence of the BEM analysis

corresponding frequency domain hydroelastic features are obtained by using the FEM and BEM respectively. The mesh size is determined by considering the convergence of the generalized added mass coefficients, given for the first platform bending and torsional modes in Figure 3.7. In the case of coarse mesh, the results are quite different due to the inadequate element size for the hydrodynamic analysis. However, the mesh size having 140, 12 and 6 elements along the *x*-, *y*- and *z*-axis, respectively, is sufficient for achieving accurate results. The diagonal added mass terms corresponding to the platform modes are presented for each incident wave direction in Figure 3.8. Although
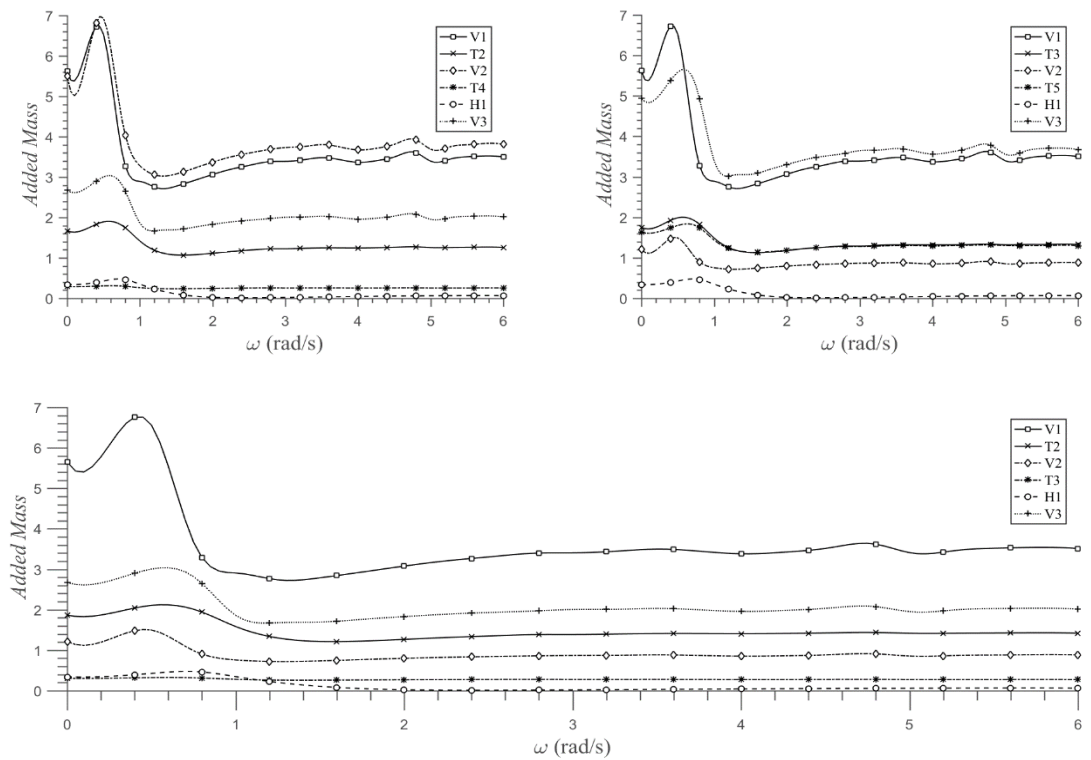
Figure 3.8 : Generalized added mass coefficients for $\alpha = 90°$ (upper-left), $\alpha = 135°$ (upper-right) and $\alpha = 180°$ (bottom).

47
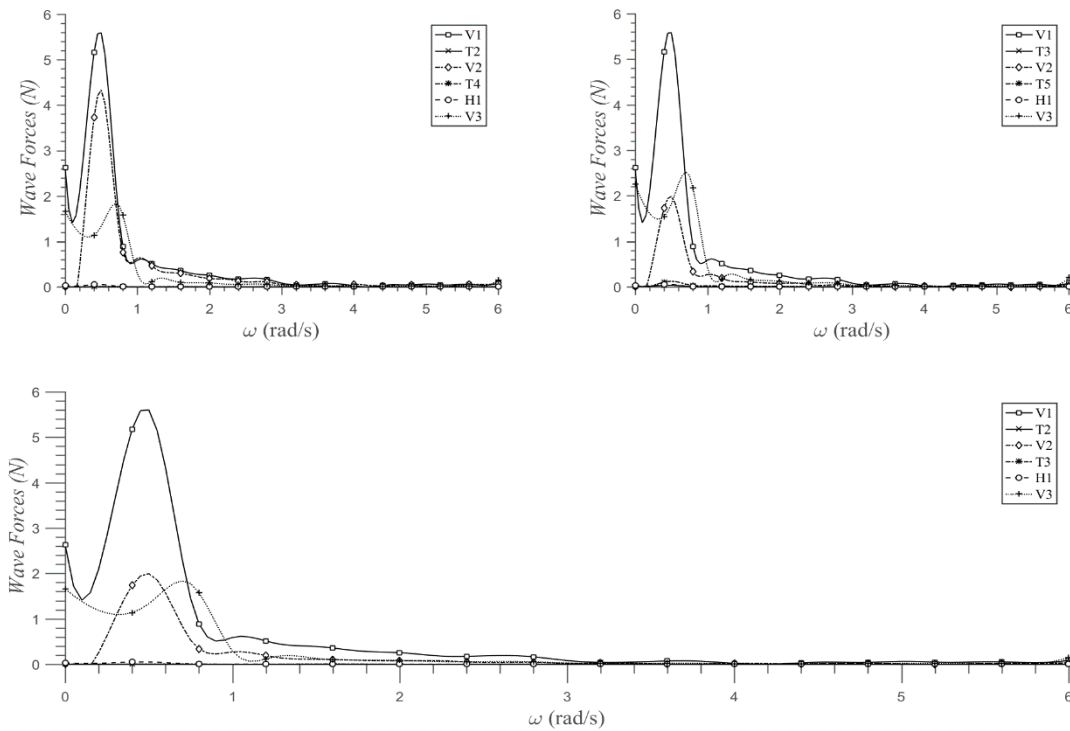
Figure 3.9 : Generalized wave excitation forces for $\alpha = 90°$ (upper-left), $\alpha = 135°$ (upper-right) and $\alpha = 180°$ (bottom).

for most of the modes the added mass coefficients of are similar despite the change in wave angle, significant variations in second and third vertical bending modes are observed.

The wave excitation forces are determined by applying the Haskind relation. As shown in Figure 3.9, the wave forces related with the vertical bending modes are relatively larger in the low frequency range, as expected. Even though the forces generally have the same amplitude, the wave force in second vertical bending mode differs for each wave angle.

The time domain fluid-structure interaction forces and excitation force are obtained from the radiation forces, i.e. added masses, and the wave excitation forces, respectively, using the Fourier transform. The Filon quadrature is adopted to integrate the oscillatory function in Eq. (2.76) for the computation of IRF. The diagonal coefficients of IRF are illustrated in Figure 3.10 for the platform modes. The coefficients of IRF are expected to decline, since the effect of the structural motions on the radiated waves decreases over time. Besides, smaller amplitude IRFs for the modes having higher natural frequency indicates that the energy transferred to the fluid are relatively small for the high frequency modes.

48
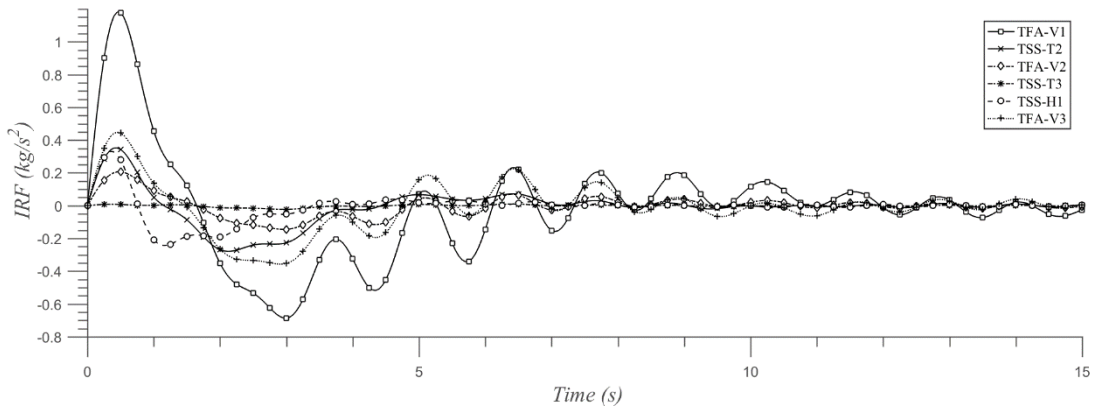
Figure 3.10 : Diagonal entries of the impulse response function (IRF) for the platform type modes ($\alpha = 180°$).

The time domain radiation forces are obtained by the convolution of the IRF. As seen in Eq. (2.75), the computation process involves the motion history of the structure. Considering that the memory effects are weakened as time progresses, however, the motion history can be limited to shorter times. Keeping the sixty seconds history is the common approach and it is adequate for achieving accurate results. The time domain radiation forces are presented in Figure 3.11 for several angles of incident wave. The forces have slightly different amplitude when the RNA is oriented according to the oblique direction (135°) of the wave-wind as a result of the modification of the tower mode shapes from FA to MX.
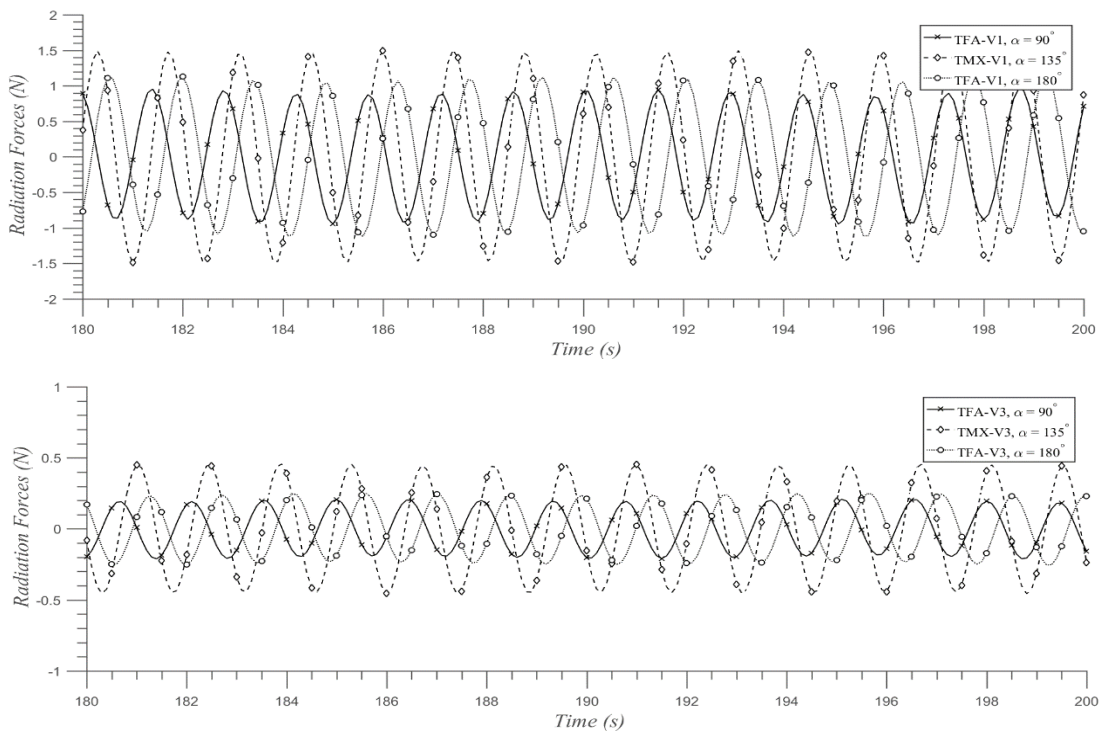

Figure 3.11 : Time domain radiation forces.

49
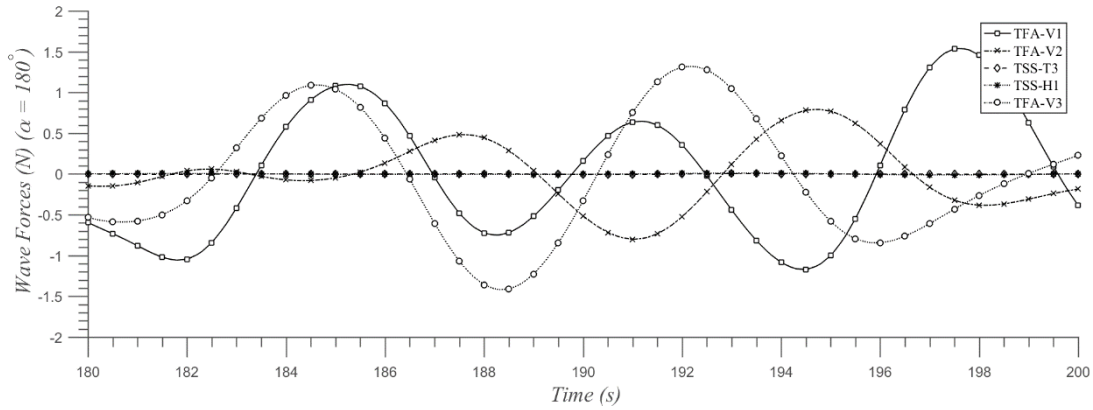
Figure 3.12 : Time domain wave forces.

The time domain wave forces are derived by the sine transformation of the frequency domain wave forces. The waves are considered as unidirectional and the wave elevation is represented by using the Pierson-Moskowitz wave spectrum. As illustrated in Figure 3.12, the magnitude of the time domain wave forces for the vertical bending modes of the platform are of higher order in parallel with the frequency domain wave forces.
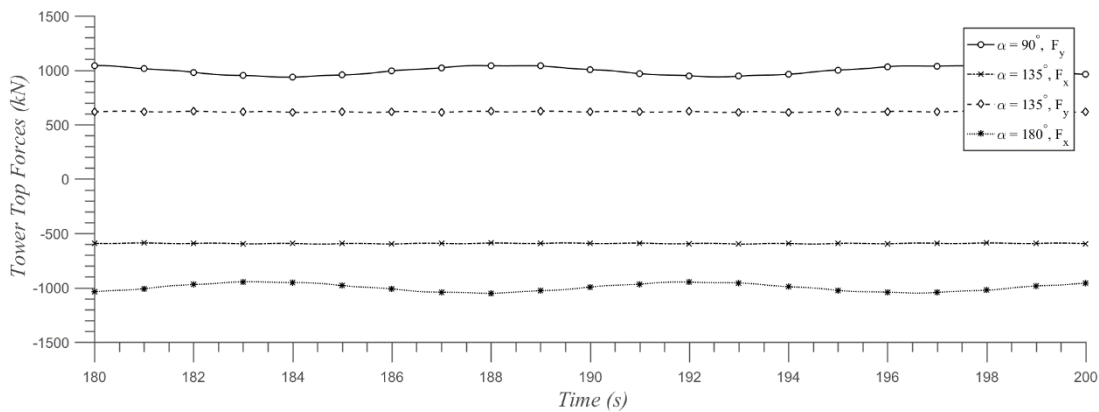
Figure 3.13 : Physical Forces on first tower top.

While applying the BEMt for the rotor aerodynamics, swirl model for the induction factor is adopted. In addition, hub-loss and tip-loss of the rotor are taken into account by using the Prandtl model. Two flapwise and one edgewise modes of the blades and drivetrain rotational flexibility are considered along with the generator degree of freedom for the structural dynamics of the rotor. The tower top forces due to rotor is presented in Figure 3.13.

The generalized aerodynamic forces are computed by substituting the tower top forces for the nodal forcing vector in Eq. (2.108). The generalized aerodynamic forces of the

50
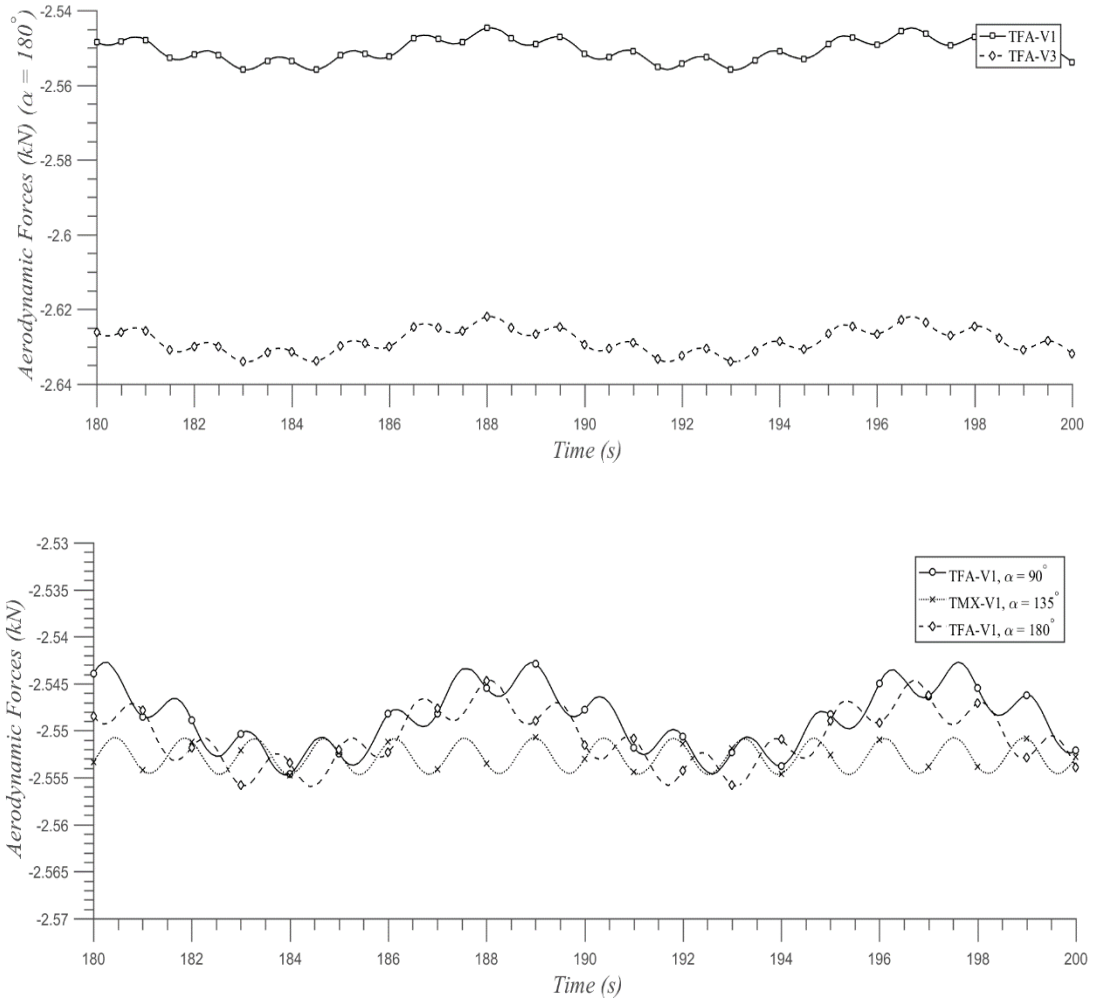
Figure 3.14 : Aerodynamic excitations in principle coordinates.

modes *TFA-V1* and *TFA-V3* are given in Figure 3.14. The aerodynamic excitation is excessively large with respect to the hydrodynamic excitation, meaning that the response is mainly due to aerodynamics. The dependence of aerodynamic excitation to the wind angle is also presented in Figure 3.14. The relation between the wave and aerodynamic excitation is revealed by the lower frequency oscillation of the aerodynamic forces about 0.14 Hz (the peak spectral frequency of the irregular waves), while the influences of the radiation forces and the rotation of the blades cause an oscillation with the blade passing frequency, 0.68 Hz. Furthermore, when the RNA is oriented to the 135° with respect to the wind angle, the influence of the wave forces over the aerodynamics diminishes for the first vertical bending mode of platform.

At last, the forces are assembled in principle coordinates and the state-space equation of motion, given in Eq. (2.111), is solved to find the principle coordinate vector representing the influences of the specified modes on overall response. The

51
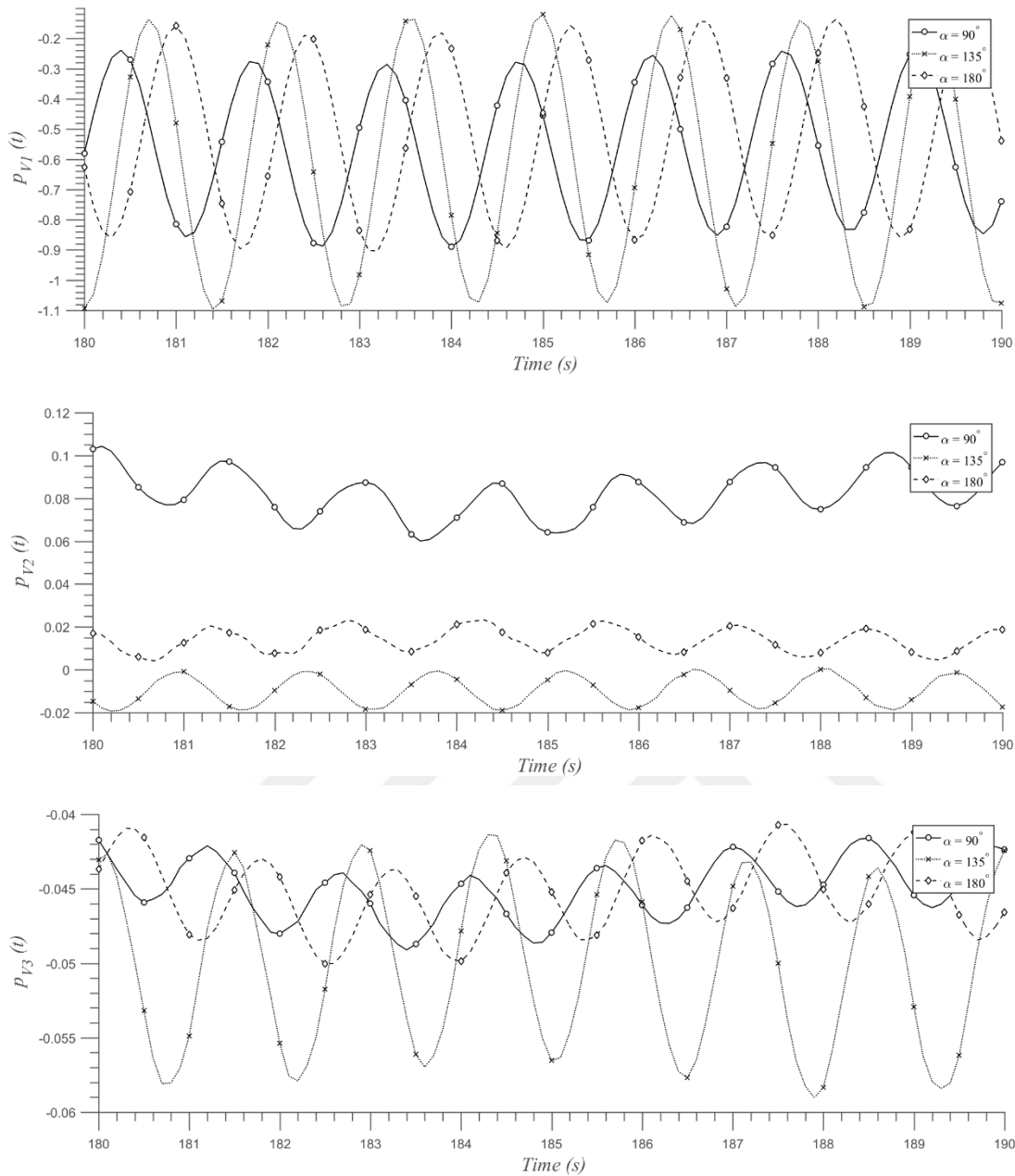
Figure 3.15 : Modal components of the response in principle coordinates.

generalized response of the platform vertical bending modes (*V1, V2* and *V3*) are demonstrated in Figure 3.15 for each environmental case. The head and beam direction of the wave-wind have same order effects on the response in symmetric vertical bending modes (*V1* and *V3*), however, for the asymmetric mode (*V2*) this correlation is vanished. The principle coordinate components for the oblique wave-wind have particular values due to different type of the tower mode shapes.

The response of the structure, i.e. nodal displacements and velocities, can be determined by converting the quantities from the principle coordinates to the physical

coordinates through the mode shapes. In Figure 3.16, the displacement of the point chosen at floater aft (-120, 0, 2) and floater fore (120, 0, 2) along with the velocities of the point (120, 0, 2) are presented for 60 s time history. The overall response is sensitive to the angle of the wave-wind. Although the minimum deflection is observed at beam direction, as seen in Figure 3.17, the most power capturing capacity is achieved by the oblique wave-wind s.
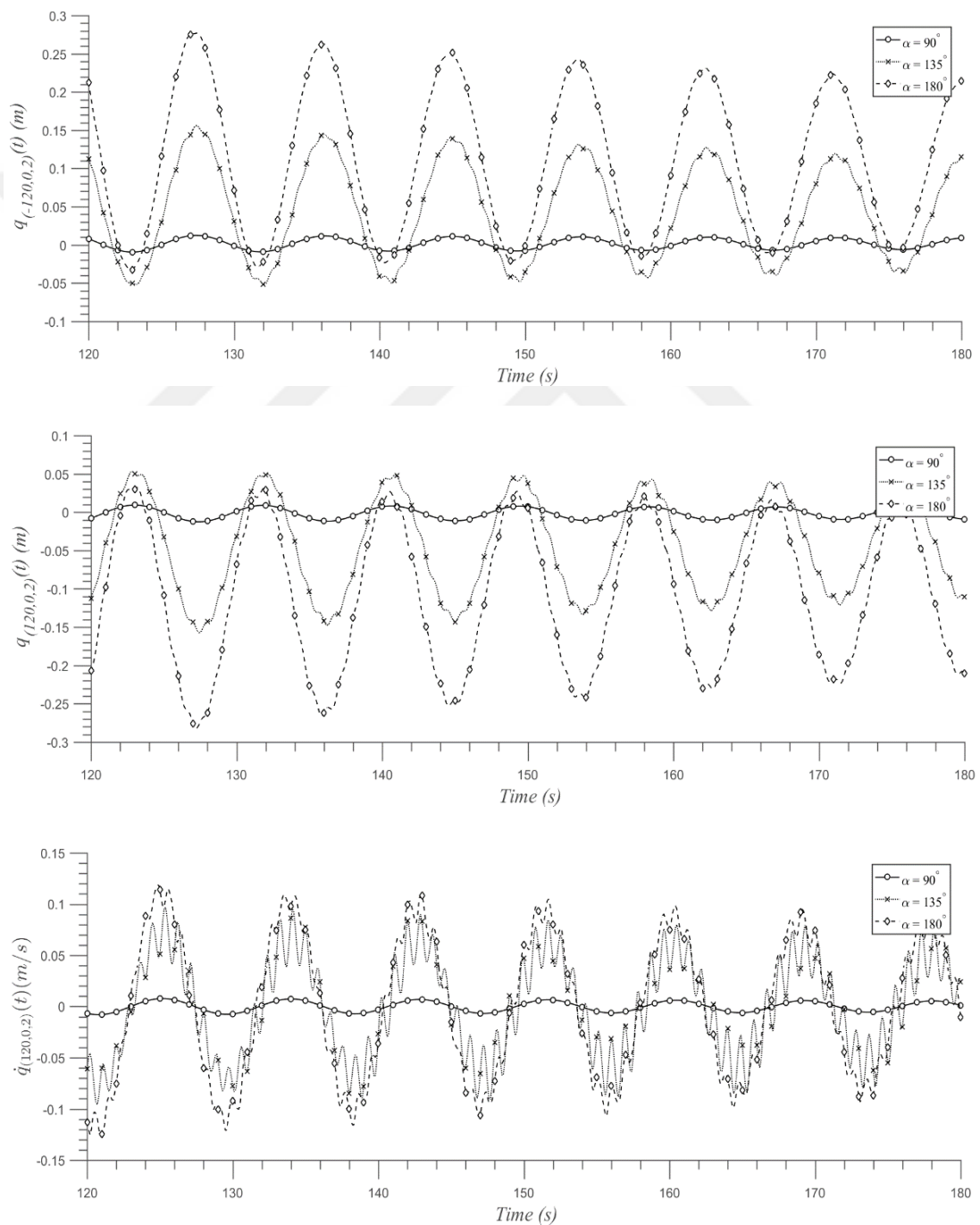
Figure 3.16 : Floater overall response.
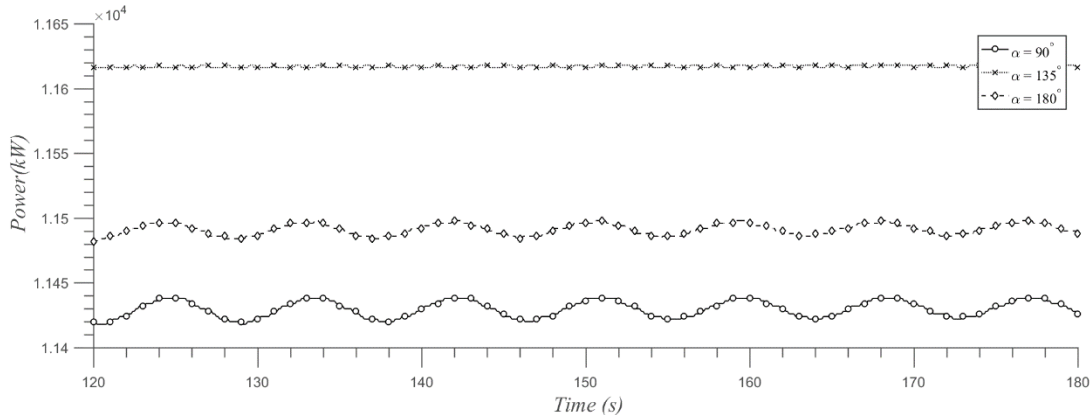
Figure 3.17 : Total generated power.

3.4 Conclusion

The time domain dynamic response of a FOWT's support structure including towers and floater is investigated under combined wave and wind loads by coupling the hydroelastic and aeroelastic solution procedures. The elastic responses of the structure is taken into account due to its relatively large dimensions. The modal approach is adopted to describe the dynamic response of the support structure and the FEM is applied to represent its dynamic characteristics, namely, the natural frequencies and corresponding mode shapes. The fluid flow, assumed ideal and irrotational, is described as the combination of potential components attributed to the wave radiation and diffraction. The fluid-structure interaction is established through the kinematical boundary condition and fluid pressure distribution over the wetted surface. The frequency domain wave radiation forces (i.e., the added mass and hydrodynamic damping effects) and wave excitation forces are determined by using a higher-order BEM approach relies on the free surface Green function, where the extended BEM formulation is adopted for removal of the frequency effects. The time domain history of the wave forces is obtained by the Fourier transformation of the frequency domain counterparts; the Filon quadrature is applied for numerical calculations.

In order to avoid detailed modelling of the structure, the FE model of the floater is constituted by using the orthotropic plate model whereas the RNAs represented by mass elements with rotational inertia on each tower top. The orientations of the mass elements are taken into consideration in the dry analysis due to the yaw degree of freedom of the RNAs.

The wave radiation and excitation forces–related with the elastic modes that induce strong fluid-structure interaction–are determined for each environmental condition and transformed to their time domain representations by the convolution of the radiation impulse response function and using the sine transformation, respectively. The aerodynamic forces due to steady wind are obtained by using the BEMt by considering the interaction with the structural motion. 2 flapwise and 1 edgewise elastic modes per blade, generator azimuth, shaft torsion, and nacelle yaw rotation are considered during the computation of the forces on each tower top. Then, the state-space formulation of the equation of motion is solved at each time step by using the 4th order Runge-Kutta method for the time integration of the responses. The general conclusions may be given as follows:

- The variation of the dynamic characteristics corresponding to the RNA orientation should be taken into account when the nacelle rotation is enabled.

- Due to the configuration of the floater, the irregular frequency effects resulting from the adopted free surface Green function is expected to be large, though the applied extended BEM formulation effectively removes the effects.

- The wave forces associated with the floater vertical bending modes have relatively higher influences over the structural response.

- The generalized aerodynamic forces are excessively large with respect to the generalized wave forces for the analyzed FOWT configuration.

- The response of the structure is mainly due to the aerodynamic excitation. Accordingly, the hydrodynamic and aerodynamic interaction forces oscillate with the blade passing frequency, which is three times of the rated rotor speed.

- The influence of the head and beam directions of the wave-wind on the response of the symmetric vertical bending modes is of the same order. The effect of the oblique wave-wind, however, can be distinctive depending on the tower mode shapes. Additionally, the correlation between the influences of the head and beam direction of the wave and wind is vanished for asymmetric floater modes.

- The overall response of the floater is minimized when the wave-wind are in the beam direction. The maximum power is generated by the oblique wave-wind case.

REFERENCES

[1] **Archer, C.L. & Jacobson, M.Z.** (2005). Evaluation of global wind power, *Journal of Geophysical Research-Atmospheres*, 110 (D12).

[2] **EWEA.** (2013). *Deep water—the next step for offshore wind energy*: The European Wind Energy Association

[3] **Athanasia, A. & Genachte, A.B.** (2013). Deep Offshore and New Foundation Concepts, *Energy Procedia*, 35, s. 198-209.

[4] **Musial, W., Butterfield, S., & Boone, A.** (2004), Feasibility of Floating Platform Systems for Wind Turbines, in *42nd AIAA Aerospace Sciences Meeting and Exhibit*. American Institute of Aeronautics and Astronautics.

[5] **Wang, C.M., Utsunomiya, T., Wee, S.C., & Choo, Y.S.** (2010). Research on floating wind turbines: a literature survey, *The IES Journal Part A: Civil & Structural Engineering*, 3 (4), s. 267-277.

[6] **Butterfield, S., Musial, W., Jonkman, J., & Sclavounos, P.** (2007). *Engineering Challenges for Floating Offshore Wind Turbines*, Conference: Presented at the 2005 Copenhagen Offshore Wind Conference, 26-28 October 2005, Copenhagen, Denmark: ; National Renewable Energy Laboratory (NREL), Golden, CO.

[7] **Ishihara, T., Phuc, P.V., & Sukegawa, H.** (2007). Numerical study on the dynamic response of a floating offshore wind turbine system due to resonance and nonlinear wave, *European Offshore Wind Conference & Exhibition*. Berlin, Germany.

[8] **Wang, C.M., Watanabe, E., & Utsunomiya, T.** (2007). *Very Large Floating Structures*, New York: Taylor & Francis.

[9] **Wang, C. & Wang, B.** (2014). *Large Floating Structures: Technological Advances*, Vol. 3: Springer.

[10] **Watanabe, E., Utsunomiya, T., & Wang, C.** (2004). Hydroelastic analysis of pontoon-type VLFS: a literature survey, *Engineering structures*, 26 (2), s. 245-256.

[11] **Suzuki, H., Yasuzawa, Y., Fujikubo, M., Okada, S., Endo, H., Hattori, Y., Okada, H., Watanabe, Y., Morikawa, M., & Ozaki, M.** (1997). Structural response and design of large scale floating structure, *Proceedings of the International Conference on Offshore Mechanics and Arctic Engineering*. American Society of Mechanical Engineers, 131-138.

[12] **Bishop, R.E.D. & Price, W.G.** (1979). *Hydroelasticity of Ships*: Cambridge University Press.

[13] **Wu, C., Watanabe, E., & Utsunomiya, T.** (1995). An eigenfunction expansion-matching method for analyzing the wave-induced responses of an elastic floating plate*, Applied Ocean Research*, 17 (5), s. 301-310.

[14] **Huang, L.L. & Riggs, H.R.** (2000). The hydrostatic stiffness of flexible floating structures for linear hydroelasticity*, Marine Structures*, 13 (2), s. 91-106.

[15] **Ertekin, R.C., Wang, S.Q., Che, X.L., & Riggs, H.R.** (1995). On the application of the Haskind-Hanaoka relations to hydroelasticity problems*, Marine Structures*, 8 (6), s. 617-629.

[16] **Lee, C.-H., Newman, J.N., & Zhu, X.** (1996). An Extended Boundary Integral Equation Method For The Removal Of Irregular Frequency Effects*, International Journal for Numerical Methods in Fluids*, 23 (7), s. 637-660.

[17] **Watanabe, E., Utsunomiya, T., Wang, C.M., & Hang, L.T.T.** (2006). Benchmark hydroelastic responses of a circular VLFS under wave action*, Engineering Structures*, 28 (3), s. 423-430.

[18] **Kara, F.** (2015). Time domain prediction of hydroelasticity of floating bodies*, Applied Ocean Research*, 51, s. 1-13.

[19] **Butterfield, S., Musial, W., Jonkman, J., Sclavounos, P., & Wayman, L.** (2005). Engineering challenges for floating offshore wind turbines, *Copenhagen Offshore Wind Conference, Copenhagen, Denmark.* Citeseer, 377-382.

[20] **Jonkman, J.M.** (2009). Dynamics of offshore floating wind turbines—model development and verification*, Wind energy*, 12 (5), s. 459-492.

[21] **Matha, D.** (2010). *Model development and loads analysis of an offshore wind turbine on a tension leg platform with a comparison to other floating turbine concepts* (NREL/SR-500-45891).

[22] **Ramachandran, G., Robertson, A., Jonkman, J., & Masciola, M.** (2013). Investigation of response amplitude operators for floating offshore wind turbines, *The Twenty-third International Offshore and Polar Engineering Conference.* International Society of Offshore and Polar Engineers.

[23] **Ma, C., Iijima, K., & Nihei, Y.** (2014). Strongly coupled method for predicting the response of flexible FOWT with mooring and its experimental validation, *ASME 2014 33rd International Conference on Ocean, Offshore and Arctic Engineering.* American Society of Mechanical Engineers.

[24] **Iijima, K., Kim, J., & Fujikubo, M.** (2010). Coupled aerodynamic and hydroelastic analysis of an offshore floating wind turbine system under wind and wave loads, *ASME 2010 29th International Conference on Ocean, Offshore and Arctic Engineering.* American Society of Mechanical Engineers, 241-248.

[25] **Jonkman, J.M.** (2003). *Modeling of the UAE wind turbine for refinement of FAST_AD* (NREL/TP-500-34755).

[26] **Jain, P.** (2011). *Wind energy engineering*: McGraw-Hill.

[27] **Yue, D.K.P.** (2005), *2.20 - Marine Hydrodynamics*, in *Massachusetts Institute of Technology: MIT OpenCouseWare*.

[28] **Newman, J.N.** (1977). *Marine hydrodynamics*: MIT press.

[29] **Ergin, A., Price, W.G., Randall, R., & Temarel, P.** (1992). Dynamic Characteristics of a Submerged, Flexible Cylinder Vibrating in Finite Water Depths*, Journal of Ship Research*, 36 (2), s. 154-167.

[30] **Wrobel, L.C.** (2002). *The boundary element method, applications in thermo-fluids and acoustics*, Vol. 1: John Wiley & Sons.

[31] **Beer, G., Smith, I., & Duenser, C.** (2008). *The boundary element method with programming: for engineers and scientists*: Springer Science & Business Media.

[32] **Brebbia, C.A., Telles, J.C.F., & Wrobel, L.** (2012). *Boundary element techniques: theory and applications in engineering*: Springer Science & Business Media.

[33] **Gaul, L., Kögl, M., & Wagner, M.** (2003). *Boundary Element Methods for Engineers and Scientists*: Springer.

[34] **Wehausen, J.V. & Laitone, E.V.** (1960). *Surface Waves*: Springer-Verlag.

[35] **Hughes, T.J.R. & Pister, K.S.** (1978). Consistent linearization in mechanics of solids and structures*, Computers & Structures*, 8 (3), s. 391-397.

[36] **Ingram, G.** (2005). Wind turbine blade analysis using the blade element momentum method. version 1.0*, School of Engineering, Durham University, UK*.

[37] **Craig, R.R. & Kurdila, A.J.** (2011). *Fundamentals of Structural Dynamics*: Wiley.

[38] **Riggs, H.R., Niimi, K.M., & Huang, L.L.** (2007). Two Benchmark Problems for Three-Dimensional, Linear Hydroelasticity*, Journal of Offshore Mechanics and Arctic Engineering*, 129 (3), s. 149-157.

[39] **Watai, R.A., Ruggeri, F., Sampaio, C.M.P., & Simos, A.N.** (2015). Development of a time domain boundary element method for numerical analysis of floating bodies' responses in waves*, Journal of the Brazilian Society of Mechanical Sciences and Engineering*, 37 (5), s. 1569-1589.

[40] **Kane, T.R. & Levinson, D.A.** (1985). *Dynamics, Theory and Applications*: McGraw-Hill.

[41] **Jonkman, J.M. & Buhl Jr, M.L.** (2005). FAST user's guide*, National Renewable Energy Laboratory, Golden, CO, Technical Report No. NREL/EL-500-38230*.

CURRICULUM VITAE

Name Surname	: Enes TUNCA
Place and Date of Birth	: Karamürsel / 1991
E-Mail	: tuncaen@itu.edu.tr

EDUCATION

- **B.Sc.**   : 2014, Istanbul Technical University

  Faculty of Naval Architecture and Ocean Engineering

  Department of Naval Architecture and Marine Engineerig

PUBLICATIONS:

- **Tunca, E., Kahraman, İ., Uğurlu, B.** 2016. Free-surface Coupled Hydroelastic Analysis Of Fluid Containers, The 30th Asian-Pacific Technical Exchange And Advisory Meeting On Marine Structures, October 10-13, 2016 Mokpo, South Korea.
- **Tunca, E., Uğurlu, B.**, 2015. Ultimate Strength Analysis For The Assessment Of Stiffener-Plate Design Configuration, The 29th Asian-Pacific Technical Exchange and Advisory Meeting on Marine Structures, October 12-15, 2015 Vladivostok, Russia.